JGR Solid Earth

RESEARCH ARTICLE
10.1029/2019JB017648

Long-Term Evolution of Nontransform Discontinuities at the Mid-Atlantic Ridge, 24°N–27°30′N

Tingting Zheng[1,2], **Brian E. Tucholke**[2], **and Jian Lin**[1,2,3]

[1]State Key Laboratory of Marine Geology, School of Ocean and Earth Science, Tongji University, Shanghai, China, [2]Department of Geology and Geophysics, Woods Hole Oceanographic Institution, Woods Hole, MA, USA, [3]Key Laboratory of Ocean and Marginal Sea Geology, South China Sea Institute of Oceanology, Chinese Academy of Sciences, Guangzhou, China

Key Points:
- Propagation of non-transform discontinuities on the Mid-Atlantic Ridge was analyzed in reconstructions of bathymetric and gravity data
- Rapid and slow propagation occurs and is controlled by magma distribution within the mantle and crust of spreading segments
- We attribute long-wavelength cross-axis asymmetry in gravity anomalies to asymmetric distribution of density anomalies in the upper mantle

Supporting Information:
- Supporting Information S1
- Movie S1
- Movie S2

Correspondence to:
J. Lin,
jlin@whoi.edu

Citation:
Zheng, T., Tucholke, B. E., & Lin, J. (2019). Long-term evolution of nontransform discontinuities at the Mid-Atlantic Ridge, 24°N–27°30′N. *Journal of Geophysical Research: Solid Earth*, *124*, 10,023−10,055. https://doi.org/10.1029/2019JB017648

Received 7 MAR 2019
Accepted 7 SEP 2019
Accepted article online 11 SEP 2019
Published online 24 OCT 2019

Abstract We studied long-term evolution of nontransform discontinuities (NTDs) on the Mid-Atlantic Ridge from 0- to ~20- to 25-Ma crust using plate reconstructions of multibeam bathymetry, long-range HMR1 sidescan sonar, residual mantle Bouguer gravity anomaly (RMBA), and gravity-derived crustal thickness. NTDs have propagated north and south with respect to flowlines of relative plate motion and both rapidly and slowly compared to the half spreading rate; at times they have been quasi-stable. Fast, short-term (<2 Myr) propagation is driven by reduced magma supply (increased tectonic extension) in the propagating ridge tip when NTD ridge-axis offsets are small (≲5 km). Propagation at larger offsets generally is slower and longer term. These NTDs can show classic structures of rift propagation including inner and outer pseudofaults and crustal blocks transferred between ridge flanks by discontinuous jumps of the propagating ridge tip. In all cases crustal transfer occurs within the NTD valley. Aside from ridge-axis offset, the evolution of NTDs appears to be controlled by three factors: (1) gross volume and distribution of magma supplied to ridge segments as controlled by 3-D heterogeneities in mantle fertility and/or dynamic upwelling; this controls fundamental ridge segmentation. (2) The lithospheric plumbing system through which magma is delivered to the crust. (3) The consequent focusing of tectonic extension in magma-poor parts of spreading segments, typically at segment ends, which can drive propagation. We also observe long-wavelength (5-10 Myr) RMBA asymmetry between the conjugate ridge flanks, and we attribute this to asymmetric distribution of density anomalies in the upper mantle.

1. Introduction

The axes of mid-ocean ridges (MORs) are offset by transform faults and nontransform offsets. Transform faults are usually >30 km long and are characterized by strike-slip faulting; shorter, nontransform offsets (second to fourth order) are more common and exhibit limited or no pure strike-slip faulting (Macdonald et al., 1991). Second-order discontinuities have offsets of ~2–30 km and can occur as oblique shear zones at slow-spreading ridges; they are quasi-stable and typically persist for a few million years or more (Sempéré et al., 1993; Spencer et al., 1997). Third- and fourth-order discontinuities have short offsets (<2 km) and are short-lived. Following Schouten et al. (1985), we refer to second- and higher-order offsets of the ridge axis as nontransform discontinuities (NTDs).

A number of NTDs have been studied at the axes of slow-spreading MORs (e.g., Gràcia et al., 2000; Parson et al., 2000; Purdy et al., 1990; Sempéré et al., 1990, 1993; Spencer et al., 1997). Crust that forms the boundaries of these discontinuities exhibits a set of features that is considered to be characteristic (see Figure 2): Inside-corner (IC) crust, bounded by the spreading axis and the active offset, is typically elevated relative to surrounding crust and often has irregular fault patterns that may be oblique to the spreading axis. Outside-corner (OC) crust is bounded by the spreading axis and the inactive trace of the offset; it is deeper, has regular, linear abyssal hills formed by inward dipping normal faults, and these abyssal hills often curve into the offset (Tucholke & Lin, 1994; Wang et al., 2015). In addition, ICs usually have elevated residual mantle Bouguer gravity anomalies (RMBA) and thus thinner crust compared to the conjugate OCs (Escartín & Lin, 1995; Tucholke & Lin, 1994).

Within NTDs at the spreading axis, ridge-like septa, domed massifs, deep valleys, or wide basins may separate the spreading ridge tips of the adjacent spreading segments (Gràcia et al., 2000; Spencer et al., 1997;

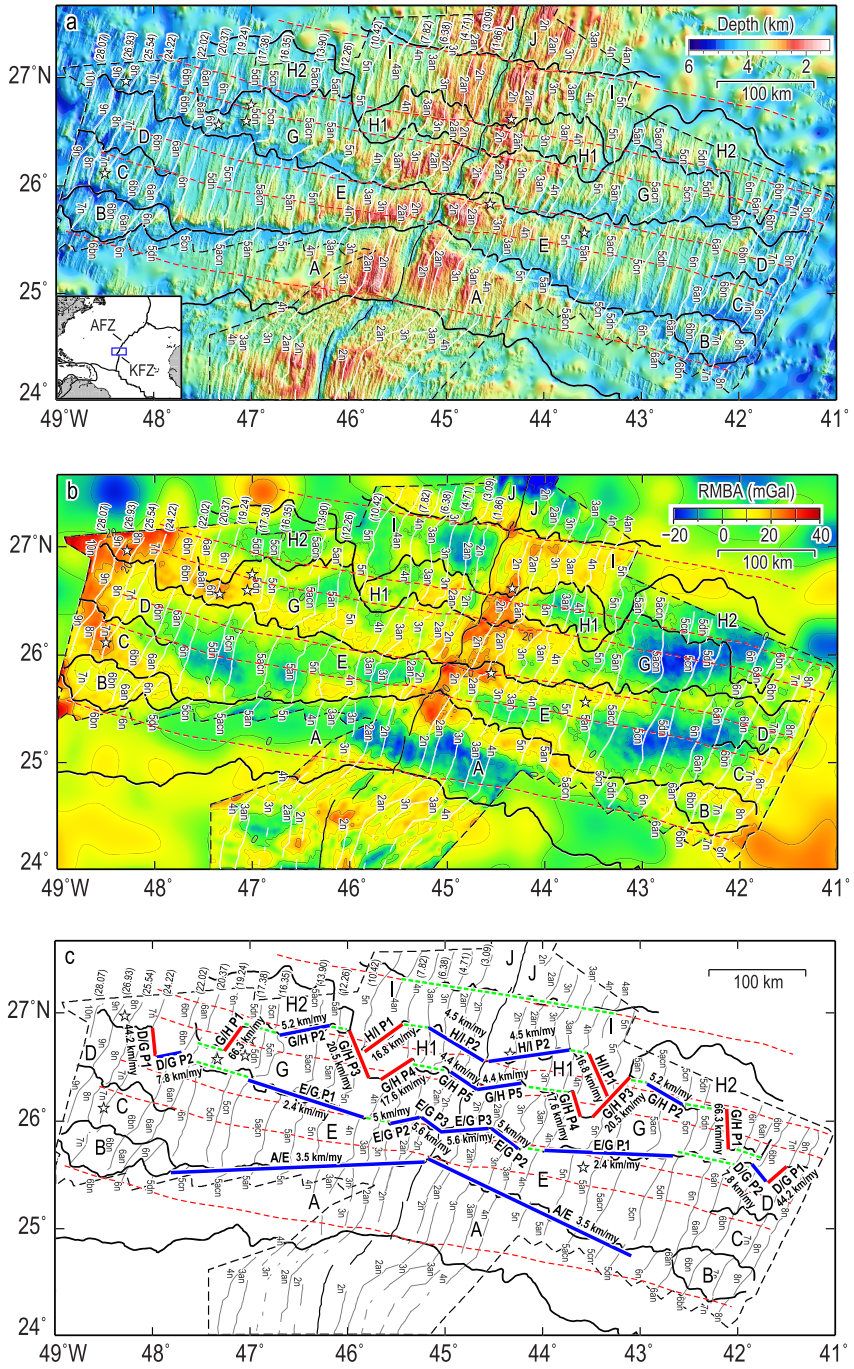

Figure 1. (a) Multibeam bathymetry of the study area (within the black dashed lines) superimposed on bathymetry derived from satellite gravity (Sandwell et al., 2014). Spreading segments are labeled from A to J. Nontransform discontinuities (NTDs) and the Mid-Atlantic Ridge (MAR) axis are shown by solid black lines. The labeled white lines are major chrons; their ages, top left, are based on Ogg (2012). The red dashed lines are calculated flowlines of relative plate motion, anchored where NTDs offset the present ridge axis. The white stars locate significant oceanic core complexes. The inset locates the study area in the North Atlantic (KFZ, Kane fracture zone; AFZ, Atlantis fracture zone). (b) Residual mantle Bouguer anomaly (RMBA) within the study area (Wang et al., 2015) superimposed on satellite-derived RMBA from Lin and Zhu (2015); the contour interval is 10 mGal. Other features are as in Figure 1a. Note the typically elevated RMBA at IC crust (mostly on south side of NTDs on eastern ridge flank, and on north side on western flank). The elevated RMBA on the east side of the ridge axis compared to the west side since Chron 3n has been attributed to asymmetric faulting (Wang et al., 2015). (c) Interpretation of long-term trends in NTD propagation with respect to flowlines of relative plate motion. Fast propagation is indicated by red lines, slow propagation by blue lines, and no propagation by green dashed lines. Propagators and rates are labeled (see also Table 2). Other features are as in Figure 1a.

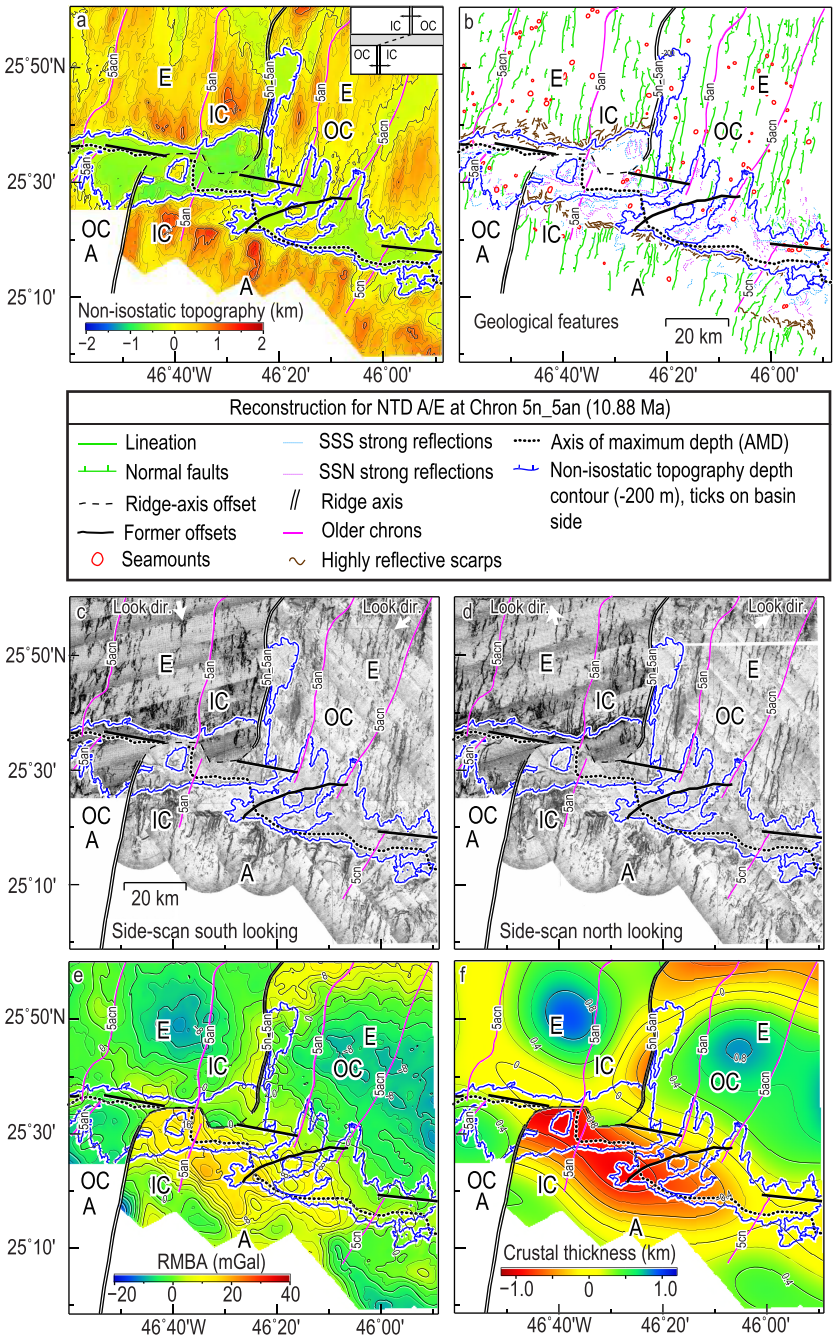

Figure 2. Example plate reconstruction of the northward propagating nontransform discontinuity (NTD) between spreading segments A and E (NTD A/E) at a time midway between Chrons 5n and 5an. (a) Nonisostatic topography, contoured at 200-m intervals. In this and following panels, the reconstructed ridge axis is a black double line and the interpreted NTD offset is a black dashed line. The solid purple and black lines show older major isochrons and their offsets, respectively. The black dotted line follows the axis of maximum depth (AMD) in the NTD. Inside corner (IC) and outside corner (OC) are labeled. Because of the northward propagation, all significant edifices observed in the NTD valley were captured from within the NTD on the western ridge flank and transferred to the east flank. Note the relatively linear, north-facing, ~east-west scarp at 25°27′N, which is interpreted to be a former transtensional plate boundary and an element of a failed rift. (b) Major geological features interpreted from multibeam bathymetry and south looking (SSS) and north looking (SSN) sidescan-sonar imagery. See legend below. (c) South looking sidescan sonar; the arrows show look direction. (d) North looking sidescan sonar; the arrows show look direction. In the sidescan-sonar images, strong backscatter is dark and weak backscatter is light. (e) RMBA, contour interval 2 mGal. (f) Modeled crustal thickness shown as departure from 6-km model thickness, contour interval 0.2 km. See Figures S20–S77 for reconstructions of non-isostatic topography, RMBA, and sidescan-sonar images (where available) for all NTDs in the survey area.

Tucholke et al., 1997). Blocky edifices can extend into the offsets from ICs. Sampling and visual observations show that these massifs may expose mantle peridotite with variable but generally minor magmatic components, indicating that tectonic extension strongly predominates over magmatic accretion, at least intermittently (Gràcia et al., 1997, 2000).

NTDs can migrate along the spreading axis, thus lengthening or shortening adjacent spreading segments and creating highly irregular off-axis traces in the ridge flanks (Gente et al., 1995; Macdonald et al., 1988, 1991; Schouten et al., 1985; Tucholke et al., 1997). Propagation of a spreading axis into an NTD is commonly observed at all MORs (e.g., Briais et al., 2002; Dannowski et al., 2018; Hey, 1977; Hey et al., 1980; Hey et al., 2010; Kleinrock & Hey, 1989; Parson & Hawkins, 1994; Pollard & Aydin, 1984). Hey (1977) proposed a rift-propagation model for intermediate-spreading ridges, showing how a propagating ridge tip can transfer crust from one ridge flank to the other, creating a V-shaped NTD trace off-axis. Spreading-center jumps and ridge reorientation have been proposed as possible causes of propagation (e.g., Hey et al., 1980; Wilson et al., 1984), and in some places propagation is related to ridge-hotspot interaction (Hey et al., 2010; Kleinrock & Hey, 1989). Seismic and gravity studies near ridge axes also suggest that at least some NTD propagation is related to increased magma supply in an adjacent spreading segment (e.g., Dannowski et al., 2018).

Among all the studies of NTDs at slow-spreading ridges, none have examined their detailed, long-term evolution in terms of the processes that have controlled their structure and along-axis migration. In this paper, we investigate these factors through a detailed study of six NTDs on conjugate flanks of the Mid-Atlantic Ridge (MAR) between 24°N and 27°30′N and in 0- to ~20- to 25-Ma crust (Figure 1). We examined multibeam bathymetry, long-range HMR1 sidescan-sonar images, RMBA, and gravity-derived crustal thickness. We made plate reconstructions of these data at the times of major magnetic anomaly chrons, plus some intermediate ages, from Chron 8n (25.54 Ma) to the present, and we analyzed NTD evolution in terms of a propagating rift model. We investigated the possible relation of magma supply to NTD propagation by analyzing magma supply within adjacent spreading segments as indicated by (1) tectonic extension (derived from fault scarps) versus magmatic extension and (2) gravity-derived crustal thickness. We find that for the conditions within our study area, NTD propagation appears to be controlled by the location and volume of magma supplied from the rising asthenosphere, modified by how the magma becomes distributed within the lithospheric plumbing system. We also observed long-term (~5-10 Myr) asymmetry of RMBA on conjugate ridge flanks in the survey area, and we hypothesize that this is caused by cross-axis asymmetry of density anomalies within the mantle.

2. Data

Our study area extends from 24°N to 27°30′N along the MAR axis and ~400 km from the axis out to ~29-Ma crust on the west ridge flank and ~370 km out to ~26-Ma crust on the east flank (Figure 1). It covers all or part of seven current spreading segments and their predecessors, separated by six NTDs. Data were acquired from four surveys described below.

2.1. Bathymetry and Nonisostatic Topography

Multibeam bathymetric data from 25°30′N to 27°N and over 0- to ~29-Ma crust on the MAR west flank were collected during the Office of Naval Research Acoustic Reverberation Special Research Program (ARSRP) in 1992 (Tucholke et al., 1997; Figure 1a). Similar data on the conjugate east flank out to ~26 Ma were acquired during the MAREAST survey in 1996 (Tucholke et al., 1996). Multibeam bathymetry from 27°N to 27°30′N and out to 12 Ma was obtained during the MODE98 cruise (Fujioka et al., 1999), and the MODE94 cruise obtained data from 24°N to 25°30′N and out to 10 Ma (Fujimoto et al., 1996). All these data were merged and gridded at a 100-m interval. We also used bathymetry derived from satellite gravity (Sandwell et al., 2014) to trace some NTDs in areas not covered by the multibeam bathymetry (Figure 1a).

We examined nonisostatic topography calculated by Wang et al. (2015) where multibeam bathymetry is available. Nonisostatic topography is derived from the bathymetric data by removing the predicted effect of plate cooling and a model of isostatically compensated topography in response to crustal thickness variations by assuming local Airy compensation. We use nonisostatic topography rather than bathymetry in our plate reconstructions to maintain visual uniformity between deep topography of older crust and shallow topography of young crust through time.

Table 1
Reconstruction Poles for Major and Interpolated Isochrons

Chron	Age (Ma)	Rotation pole			STD (km)[b]
		Lon. (°N)	Lat. (°E)	(°)[a]	
2n	1.86	74.71	47.17	−0.43	2.63
2an	3.09	76.74	46.9	−0.67	2.56
3n	4.71	59.57	−34.77	−1.7	6.2
3n_3an[c]	5.55	64.56	−30.78	−1.77	3.12
3an	6.38	69	−25.6	−1.85	3.76
4n	7.82	76.57	−10.38	−2.04	2.75
4n_5n[c]	9.55	76.42	92.96	−2.18	4.69
5n	10.42	68.68	108.59	−2.35	3.48
5n_5an[c]	10.88	66.95	10.1	−2.45	5.02
5an	12.26	62.48	112.82	−2.76	3.68
5acn	13.9	73.43	98.78	−3.31	2.81
5acn_5cn[c]	15.13	74.46	95.88	−3.66	2.91
5cn	16.35	75.28	93.18	−4.01	4.33
5dn	17.38	70.99	102.68	−4.27	2.81
6n	19.24	79.97	22.63	−5.44	10.6
6an	20.37	79.9	38.79	−5.68	5.94
6bn	22.02	78.9	62.28	−5.9	3.67
7n	24.22	79.17	29.37	−6.87	3.39
8n	25.54	78.94	30.57	−7.18	2.32

[a]Negative rotations are clockwise rotations of the east ridge flank to the west flank. [b]STD is standard deviation that estimates average fitting errors by measuring distances between the rotated western end points of the east-flank Kane and Atlantis fracture zones and the west-flank traces of the fracture zones. [c]Interpolated midpoint between isochrons, assuming constant spreading rates.

2.2. Gravity and Crustal Thickness

Shipboard gravity data were collected during the four surveys noted above (Figure 1b). Wang et al. (2015) used those data to calculate residual mantle Bouguer anomaly (RMBA) and to derive model crustal thickness, both of which we used to evaluate the structure and evolution of NTDs. RMBA from global satellite data (Lin & Zhu, 2015) was incorporated in the region surrounding the survey. These data were merged with shipboard RMBA using a Gaussian best fit between shipboard and satellite-derived RMBA within the study area (Figure 1b).

2.3. Magnetic Anomalies and Spreading Rates

Magnetic anomaly identifications (Figure 1) were taken from studies of the ARSRP and MAREAST surveys (Tivey & Tucholke, 1998; Tucholke et al., 1996, 1997), the area north of 27°N (Fujioka et al., 1999), and the survey at 24–25°N (Tivey et al., 1998). Anomaly ages were assigned from the geomagnetic polarity timescale of Ogg (2012). Average half spreading rates in the study area were about 13–16 km/Myr before ~19 Ma, increased to ~20 km/Myr at 18 Ma, and then steadily decreased to ~10 km/Myr at present (Wang et al., 2015).

2.4. Long-Range HMR1 Sidescan-Sonar Images

The ARSRP and MAREAST surveys obtained long-range (~8–10 km) HMR1 sidescan-sonar images (Rognstad, 1992; Figures 2c and 2d, and S20–S71 in the supporting information). Ship tracks in those surveys were oriented oblique to the spreading direction and were spaced 4–9 km apart, widening with distance (and thus seafloor depth) away from the ridge axis. This provided sidescan coverage >110% in each of two look directions ("north" and "south") and thus insonified seafloor features that face both toward and away from the ridge axis. The sidescan images show small-scale details of geological features that cannot be observed in the multibeam bathymetry.

3. Methods

3.1. Plate Reconstruction and Plate Flowlines

To study the evolution of the NTDs through time, we derived a series of 19 plate reconstruction poles from Chron 8n (25.54 Ma) to the present (Table 1 and Figures S1-S19). These were derived for 15 major chrons plus four crustal ages interpolated between chrons.

The reconstruction poles were derived using two simultaneous constraints: (1) matching magnetic anomalies of the conjugate ridge flanks and (2) matching the traces of the Atlantis and Kane fracture zones that lie north and south of the survey area (Figure 1), respectively. Each reconstruction was based on the best visual fit of these features. Magnetic anomalies on conjugate ridge flanks rarely match exactly because of asymmetric tectonic extension and tectonic rotation near and within NTDs that can affect the local orientation of crustal magnetization. Therefore, some overlaps and underlaps are inevitable. All reconstructions rotated the east ridge flank to the fixed west flank (Figures S1-S19).

Using the derived poles, we made reconstructions of nonisostatic topography, RMBA, and sidescan-sonar imagery (where available; Figures 2 and S20–S77). We defined a cutting line that best accommodates data from both ridge flanks, taking into consideration data in areas of underlap and overlap in the following steps: (1) splitting any difference between the conjugate magnetic anomalies, (2) adjusting a cutting line between east and west flank data according to topography so as to avoid sharp depth variation between conjugates, and (3) using sidescan-sonar imagery (both north and south looking) for further small-scale adjustment. The first step above is objective, while the last two steps subjectively reduce any major visual disparities in depth and structure between the conjugates. Where interpreting the ridge-axis offset within an NTD, we also matched the conjugates by avoiding sharp variations in topography.

We calculated flowlines of relative plate motion from the derived reconstruction poles (Figure 1) to provide more detail than was available in previous studies (e.g., Klitgord & Schouten, 1986). Calculated differences between the traces of NTDs and reference flowlines were used to evaluate the along-axis migration of NTDs through time.

3.2. Identification of Nontransform Discontinuities

We name NTDs according to their bounding spreading segments, for example, NTD A/E is between segments A and E. We defined the traces of NTDs primarily by following the axis of maximum depth (AMD) between spreading segments, with additional constraints from offsets of crustal isochrons across the discontinuities (Figure 1). For some areas where multibeam bathymetric data are not available, for instance at the northern and southern edges of the study area, we used bathymetry derived from satellite gravity to estimate the position of the AMD. Some NTDs have had temporary, small to zero offsets of the ridge axis where volcanic ridges may be more or less continuous across the NTD between adjacent segments; in these cases we used intermittent basins and other minor structures to estimate NTD position, linking the AMD in the older and younger NTD valley. We note that the AMD is only an approximation and not an exact trace of a former tectonic offset of the ridge axis within an NTD.

We redefined the NTD between segments H and I compared to Tivey and Tucholke (1998) and Wang et al. (2015) by dividing segment H into two parts. One segment (H2) extends from Chron 6bn or older to Chron 5an/5n. Segments G and I were juxtaposed for a short time (~1.5 Myr) before the segment (H1) was reestablished, extending to the present ridge axis.

3.3. Crustal Age Interpolation

We interpolated the crustal age from magnetic anomalies into a 400-m spacing two-dimensional grid. We assumed constant spreading rates between major identified magnetic anomalies and used an average plate-spreading direction of N103.5°E. To evaluate errors in the calculated crustal age grid, we calculated the root-mean-square misfit between the original magnetic anomalies and crustal ages in the grid; the calculated RMS misfit for all isochrons does not exceed 0.07 Myr.

3.4. Calculation of Tectonic and Magmatic Extension

To investigate whether NTD migration is related to magma supply within adjacent spreading segments, we calculated tectonic and magmatic extension through time in each segment (Figure 3). Plate separation at the spreading axis is the sum of a magmatic component (as reflected by M factor = magmatic component/total plate separation), in which space is filled with magma, and a tectonic component (T factor) in which space is created by extensional faulting. We derived an approximation of T factor from the accumulation of observed heave on normal faults and assumed that the correlative $M = (1 - T)$ is a reasonable approximation of magmatic input at the ridge axis. The M factor probably is not an absolute value of magmatic extension; however, it serves our purpose because we use it to compare *relative* magmatic extension between segments.

To derive the T factor, we determined from multibeam bathymetry the topographic slopes that face the ridge axis within an azimuth of 20° from the spreading direction. We consider these slopes to represent heave on inward-facing normal faults. Careful analysis of the sidescan-sonar imagery shows that outward-facing slopes on the ridges associated with these inward-facing faults almost always have small seamounts and hummocky volcanic topography on their surface (e.g., Figures 2b–2d), and thus, they are the back-tilted surfaces of fault blocks. Therefore, the extent of inward-facing slopes is a good approximation of tectonic extension.

We limited derivation of the T factor to the parts of spreading segments away from the irregular margins of NTDs because those margins can have slopes that are strongly affected by mass wasting and tectonism within the NTDs (Figure 2). Within each segment, we defined elongated, isochron-parallel boxes of a given cross-isochron width, starting from the ridge axis and extending onto each ridge flank (e.g., the red box in Figure S78). The along-isochron box length was limited by lines that separate normal abyssal hill-structure from irregular structure at the margins of NTDs. Box length was oriented N13.5°E, perpendicular to average plate flowline direction and parallel to abyssal hills.

We calculated tectonic extension (T) inferred from inward-facing slopes within boxes as $T = (\text{area with slope} > \alpha)/(\text{total area})$, where α is slope in degrees. To examine T versus age, we stepped the boxes along the flowlines with varying overlap distance to get running averages. We tested box widths ranging from 5 to 20 km in

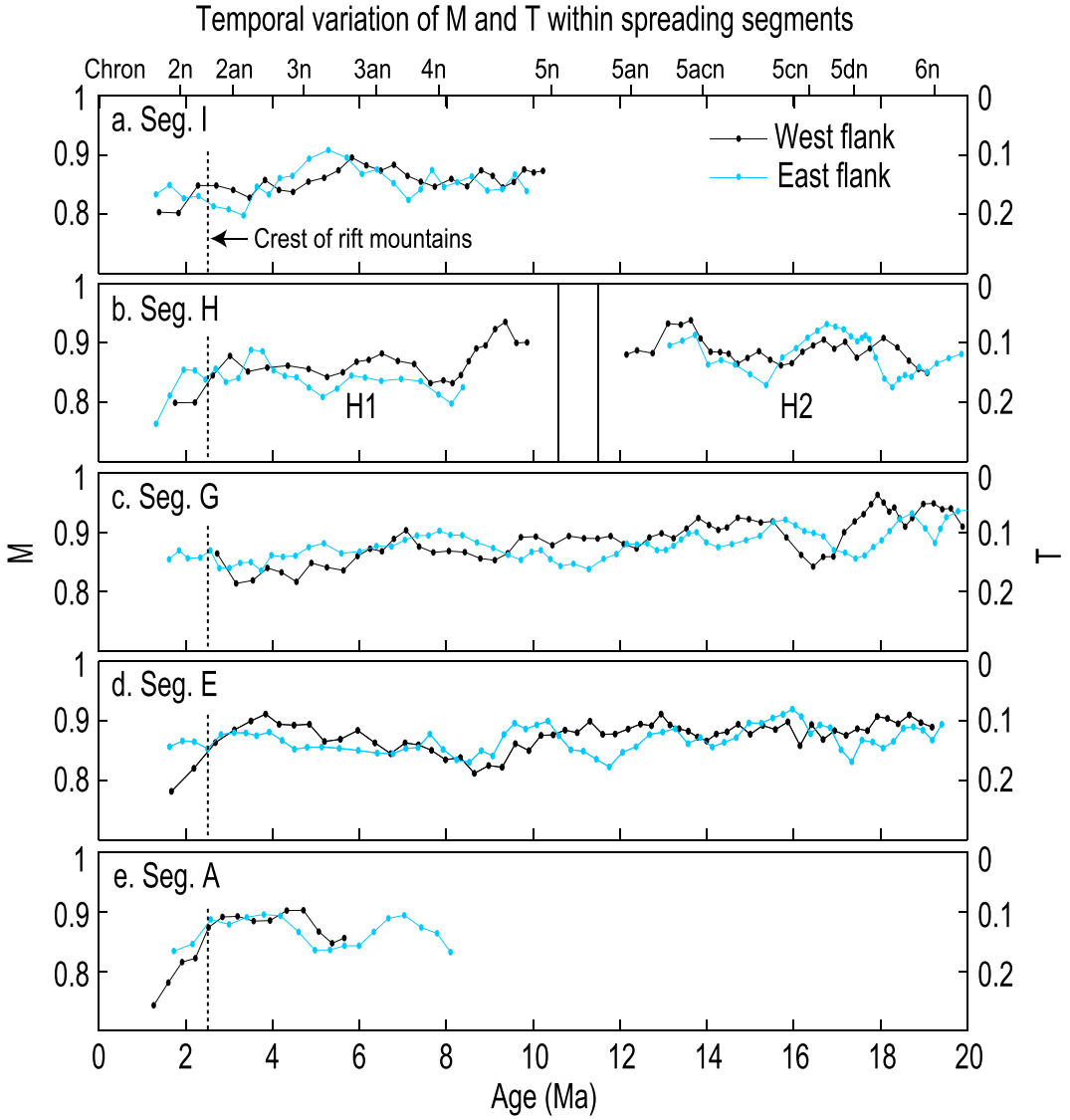

Figure 3. Fractional magmatic extension (M, left axis) calculated from tectonic extension (T, right axis) versus time for conjugate ridge flanks of five spreading segments within the study area. Each point is an average value within a 20-km-wide box, as shown in Figure S78, with box steps of 4 km (80% overlap). See text for explanation. Note that most values vary independently between conjugate flanks due to asymmetric faulting at the ridge axis, and they also are independent from segment to segment. The black dotted line at ~2.5 Ma marks the approximate crest of the rift mountains bordering the axial rift valley.

5-km increments, overlaps of 20 to 80% in 20% increments, and slopes from >5 to >30° in 5° increments. For the same overlap (80%) and slope values (>5°), larger box width results in a smoother curve for T versus age and thus misses detailed short-wavelength information (Figure S79). A greater percent overlap reduces the information content (Figure S80). The dominant wavelength of abyssal hills along flowlines is ~5 km; thus, a 5-km box width results in aliasing. T and M values derived from slopes ranging from >5 to >30° show similar patterns, but their amplitudes decrease with increasing minimum slope values (Figure S81). Taking all these effects into consideration, we selected a 20-km wide box with steps that create 80% overlap and slopes >5° to depict tectonic extension exhibited by inward-facing normal faults.

To investigate relations between T (and thus M) and other data within spreading segments, we calculated average crustal age within each overlapping box, as well as average value of bathymetric depth, nonisostatic depth, RMBA, and crustal thickness on each ridge flank (Figures S82–S86).

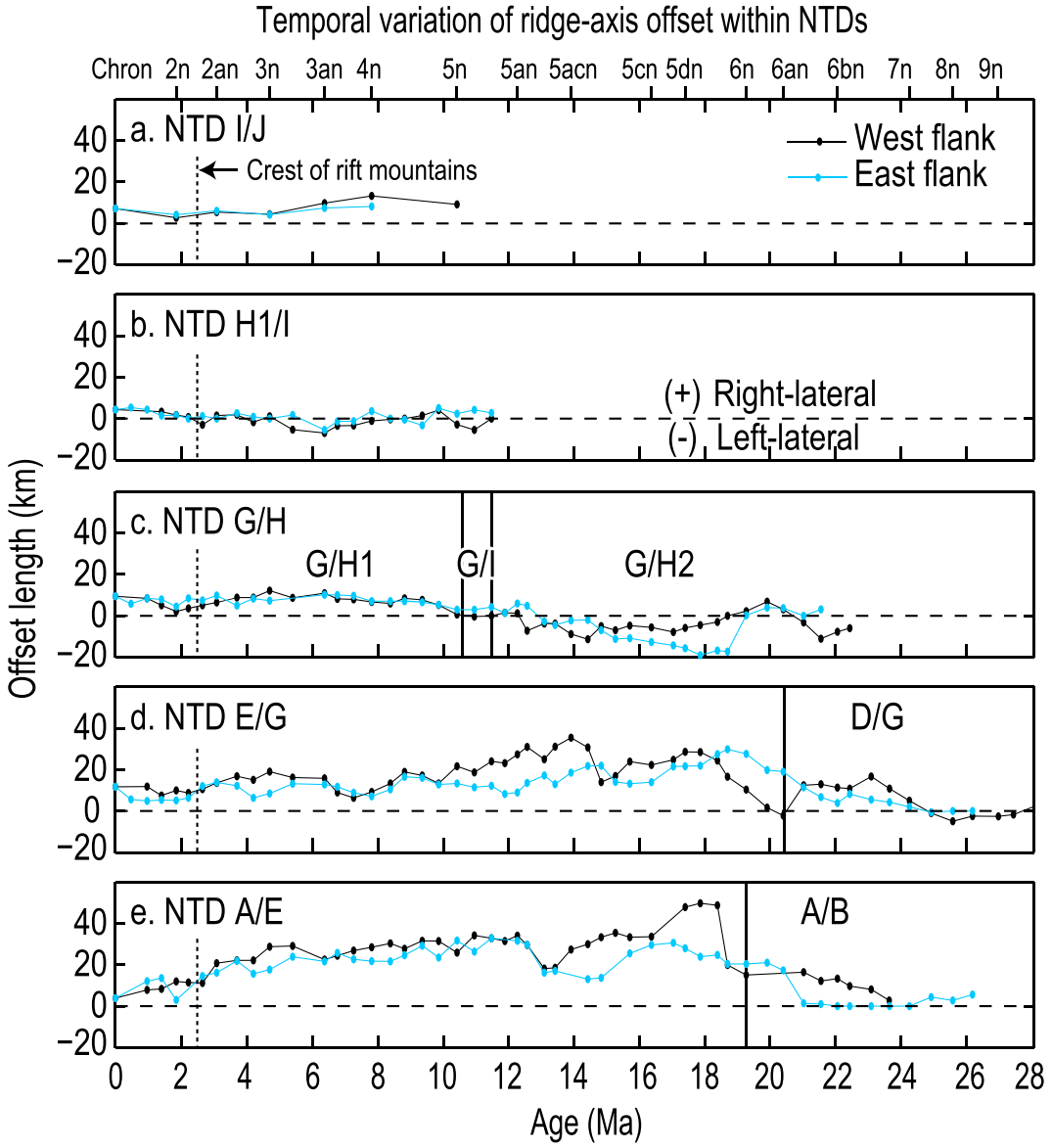

Figure 4. Magnitude of ridge-axis offset within NTDs versus age for conjugate ridge flanks. See text for explanation. Positive values are right-lateral offsets, and negative values are left-lateral. Differences in offset between conjugate ridge flanks are discussed in the text. The black dotted line at ~2.5 Ma marks the approximate crest of the rift mountains bordering the axial rift valley.

3.5. Offset and Age of NTDs

We calculated the magnitude of isochron offsets at NTDs A/E through I/J to investigate their variation through time and possible relation to propagation rate (Figure 4). Isochron positions in segments were determined by following abyssal hill trends. There are significant differences (~20 km) in apparent offset between conjugate ridge flanks in some places. We attribute these to (1) straight-line projection of age to NTDs, which does not follow any curvature in isochrons; (2) the variable and sometimes poor quality (and thus accuracy) of anomaly picks in this slow-spreading crust; and (3) asymmetric spreading and tectonic rotation of crustal blocks. We minimize these differences by using the average offset of the two ridge flanks in our analyses. The age of an NTD at any location was taken to be the midpoint of the offset of an isochron as determined above.

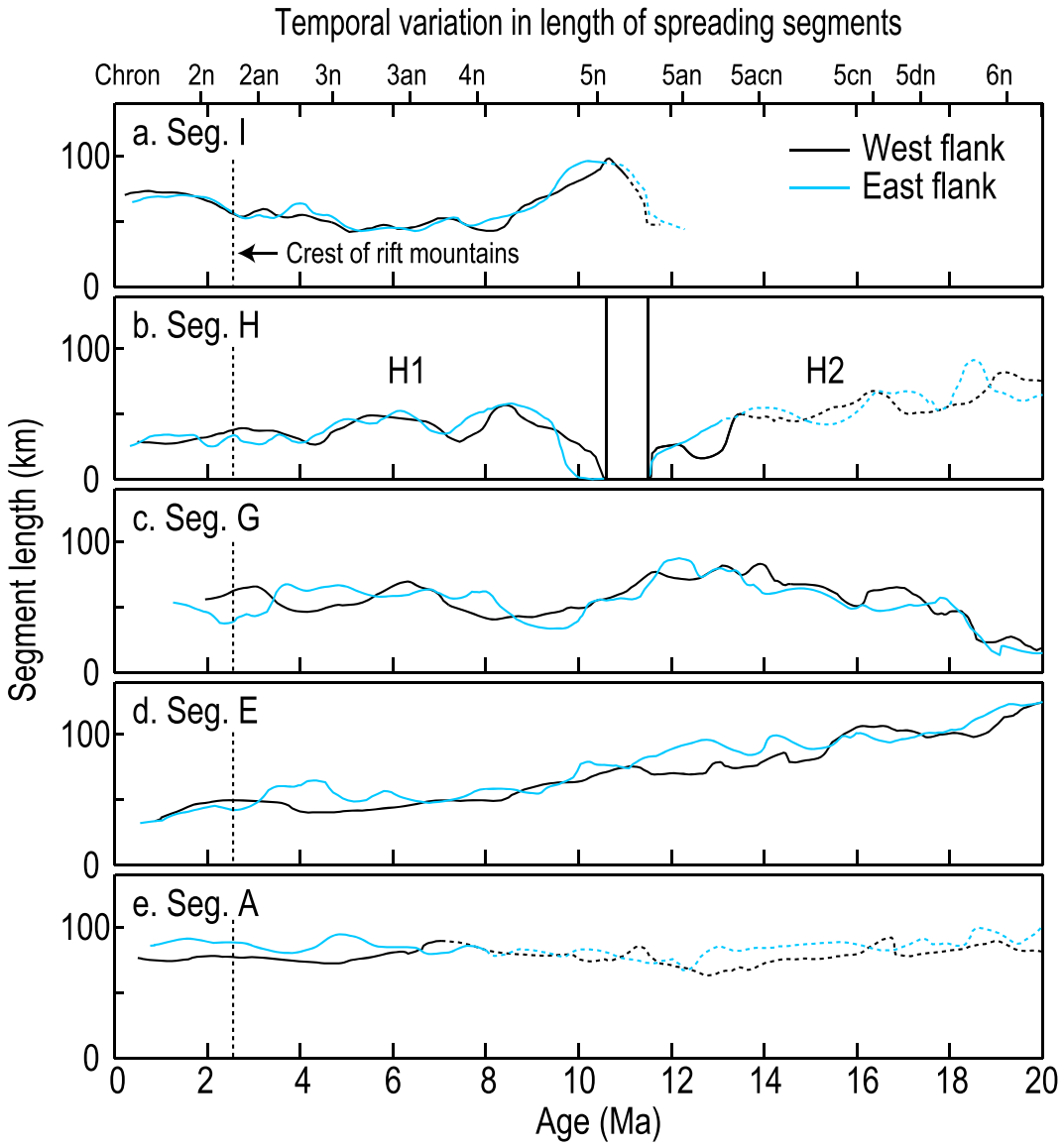

Figure 5. Length of spreading segments versus age for conjugate ridge flanks. Lengths are measured between the axes of maximum depth (AMDs) that bound the segments. See text for explanation and for discussion of differences between conjugate ridge flanks. The dotted lines in segments A, H2, and I are based on AMDs picked from lower-resolution satellite-derived bathymetry outside our survey area.

3.6. Segment Length and Propagation

We calculated ridge-segment length between the AMDs of NTDs that bound segments on both ridge flanks along an azimuth of N13.5°E (i.e., perpendicular to flowlines; Figure 5). We used average ages in 5-km-wide boxes with 80% overlap and calculated segment length between AMDs at the midpoints of the boxes at each step. We also determined quantitatively how NTDs migrate along the ridge axis through time by calculating distances of their AMDs from reference flowlines, with the reference flowlines anchored where they presently intersect the ridge axis (Figure S87).

4. Results

4.1. Pattern of NTD Evolution

NTD traces have varied from being quasi-stable to migrating along the spreading axis over both short and long periods (Figure 1). NTD C/D disappeared following Chron 6an, ~22 Ma, apparently in response to a

change in relative plate motion. NTDs A/B and B/E permanently merged into NTD A/E within 1–2 Myr thereafter (Tucholke et al., 1997). NTDs G/H2 and H2/I merged briefly following Chron 5an, ~12 Ma, and then reappeared as NTDs G/H1 and H1/I near Chron 5n, ~10 Ma. Because of these changes and other NTD migration, segment lengths have changed significantly through time.

The vast majority of ridge-axis offsets within the NTDs of the study area have been right lateral. Several NTDs persisted through zero offset, at which times they showed little or no topographic expression (e.g., NTDs H1/I and I/J since Chron 2an, ~3Ma; Figure 1a). Averaged for conjugate ridge flanks, offsets have ranged from 0 to a maximum of ~37 km (Figure 4); sometimes when the offset was small, it temporarily reversed to left lateral (e.g., NTD G/H2 at Chrons 5dn and 5cn). Nonetheless, all NTDs and the adjacent ends of their bounding segments tend to show a set of common features, summarized below.

4.2. General Characteristics of NTDs

Characteristic IC/OC structure of segment ends that bound the NTDs in our study area is well developed. IC crust typically exhibits elevated, blocky edifices that average 600–700 m higher than OC crust on the opposite side of the NTD or the ridge axis (Figures 6, 7, and S20–S77). Topography of these blocks usually is more complex than that of OC crust; ridge-parallel abyssal hills bounded by normal faults that dip toward the ridge axis are mostly present at ICs, but they are commonly disrupted by more irregular normal faults. Slopes of the NTD walls at ICs are relatively steep (up to 40°) and break abruptly from the IC highs. The IC crust generally has higher values of RMBA than OC crust (Figures 1b and S20–S77), implying thinner crust. In contrast to ICs, OC crust usually exhibits long, linear abyssal hills that deepen gradually into the NTD. Some abyssal hills curve toward the ridge axis within the NTD, reflecting rotation of the stress field at the ridge-axis offset.

Well-defined NTD valleys are developed where ridge-axis offsets exceed ~5 km; they typically are ~600 to 900 m deeper than crust in segment centers and have widths of ~8–25 km. A few NTDs such as A/E on the west ridge flank, and I/J, have quasi-linear traces, with the AMD varying less than ~5 km from the long-wavelength trend of the NTD. However, most AMD traces are more irregular, showing excursions of 10 to 20 km. As ridge-axis offsets decrease below ~5 km, the topographic valley of an NTD generally disappears and abyssal hills extend across the discontinuity. In such cases an NTD can be inferred only by relative depression of the abyssal hills, by continuity of a series of deeper basins between abyssal hills, and in some cases by elevated RMBA along the NTD.

The continuity of NTD valleys can be interrupted by major edifices. These may be attached to crust on either side of the NTD, or they may form continuous septa that extend across the NTD valley. In a few places there are isolated edifices within the NTD valley that have no topographic connection to either IC or OC crust (e.g., Figure 6b). The edifices are similar to septa and massifs that occur between offset ridge tips in NTDs at the present ridge axis (Spencer et al., 1997; Gràcia et al., 2000). Long-range sidescan-sonar data show that the edifices usually have irregular, lumpy surface texture and occasional small volcanic cones with diameters of a few hundred meters up to a kilometer or more, suggesting that they are primarily of volcanic origin. Occasional volcanic cones are also scattered elsewhere within the NTDs.

Some details of tectonic structure within NTD valleys can be interpreted from the sidescan-sonar images, although with greater crustal age, these are increasingly obscured by sediment cover and mass wasting of steep slopes. Edifices in the valleys often have randomly oriented, small-scale, irregular scarps, and a few have long, straight, relatively smooth scarps along their margins (e.g., Figures 2 and S21). These scarps are typically rotated ~20–50° clockwise with respect to the ridge-axis orientation, similar to orientations of fractures and scarps observed in ridge-axis NTDs on the MAR north of our survey area (Gràcia et al., 2000). Some studies (e.g., Wetzel et al., 1993) have found evidence for bookshelf faulting within NTDs. If such faulting was occurring at the typical right-lateral offsets in our study area, we would expect faults to be oriented counterclockwise to the ridge axis, which we do not observe. Thus, we interpret the observed scarps to be fossil transtensional faults that previously offset the ridge tips of the adjacent spreading segments and that have experienced little or no rotation.

Magmatic crust generally is thinner and more discontinuous at segment ends and within NTDs than it is at segment centers (e.g., Lin et al., 1990), which can result in gabbro and ultramafic rocks being exposed at the NTDs (e.g., Cannat et al., 1995; Gràcia et al., 2000). Outcrops of these rocks have been identified where RMBA is elevated in NTDs both on- and off-axis in slow-spreading ridges (e.g., Cannat et al., 1995;

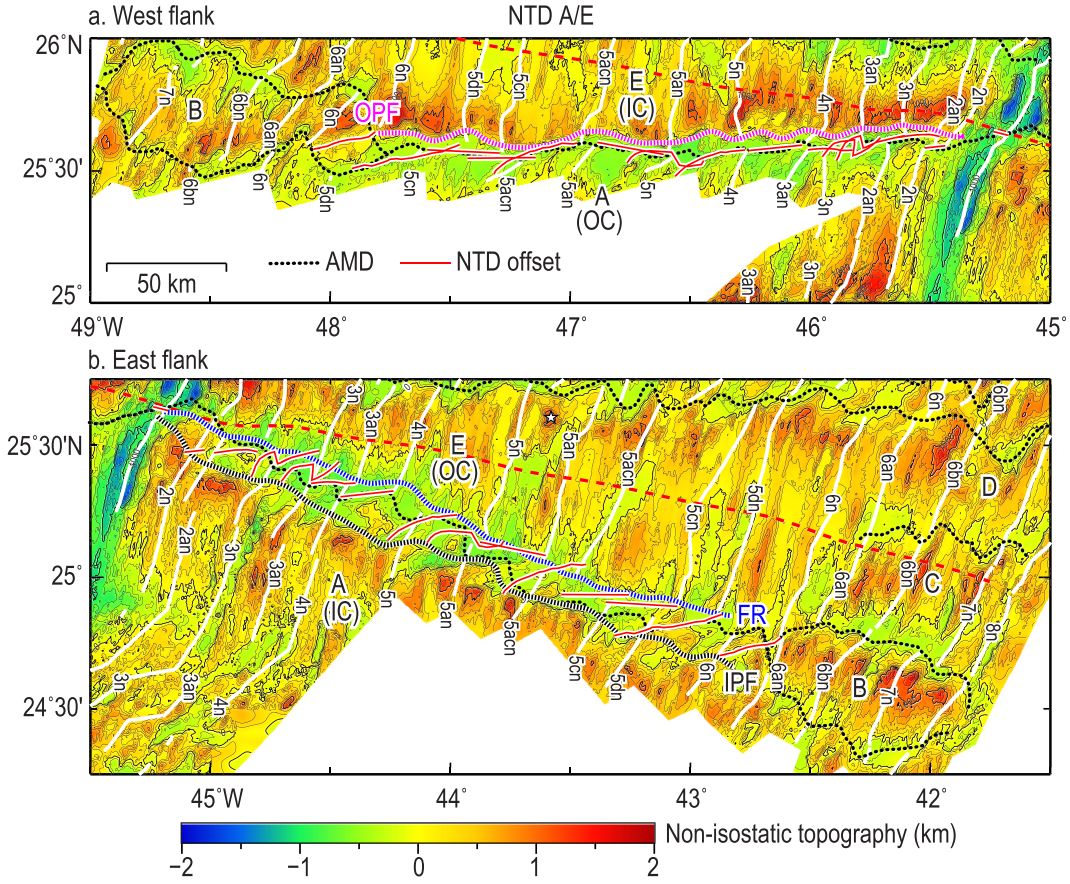

Figure 6. Nonisostatic topography of the northward-propagating nontransform discontinuity (NTD) A/E on (a) the west flank and (b) the east flank of the MAR. Contour interval is 200 m. Inside corner (IC) and outside corner (OC) crust is labeled; isochrons are labeled white lines, flowlines of relative plate motion are shown by red dashes, axes of maximum depth (AMDs) of NTDs are black dotted lines, and former ridge-axis offsets within the NTD are shown as red lines. The outer pseudofault (OPF), inner pseudofault (IPF), and failed rift (FR) of the propagating NTD are shown by red, black, and blue closely dashed lines, respectively. The former ridge-axis offsets are from plate reconstructions in Figures S20 to S35; because those reconstructions were made only at specific chrons, the offsets should not be considered to represent a definitive set of northward jumps of the propagating ridge tip.

Paulatto et al., 2015). Similarly, RMBA normally is elevated at ICs and partially into the adjacent NTDs in our study area (Figure 1b), suggesting that lower crust and upper mantle may be exposed on the IC margins of the NTDs. At this time, no samples exist to test this.

The occurrence and distribution of the structural and gravity features noted above generally relate to the stability or along-axis migration of the NTDs. Below, we discuss the NTDs within this framework.

4.3. NTD at the Southern Edge of Segment A

The NTD at the southern edge of segment A propagated quasi-regularly northward ~80 km from about Chron 7n (~24 Ma) to Chron 2an (~3 Ma) at a rate of ~3.8 km/Myr, but it has been stable since ~Chron 3n (Tucholke & Schouten, 1988; Figure 1). Detailed multibeam bathymetry of this NTD is available only for crust younger than about Chron 3an. Over this period the offset of the ridge axis has been right lateral and apparently small, less than a few kilometers, although the offset recently increased to ~18 km. At least since Chron 3an, the northern NTD margin exhibits classic IC morphology on the west flank (Figure 1a). Internally, segment A on the north side of the NTD has some of the lowest RMBA values within the study area (i.e., normal to thickened crust; Figure 1b) and as a consequence mostly exhibits linear, closely spaced abyssal hills (Shaw & Lin, 1996).

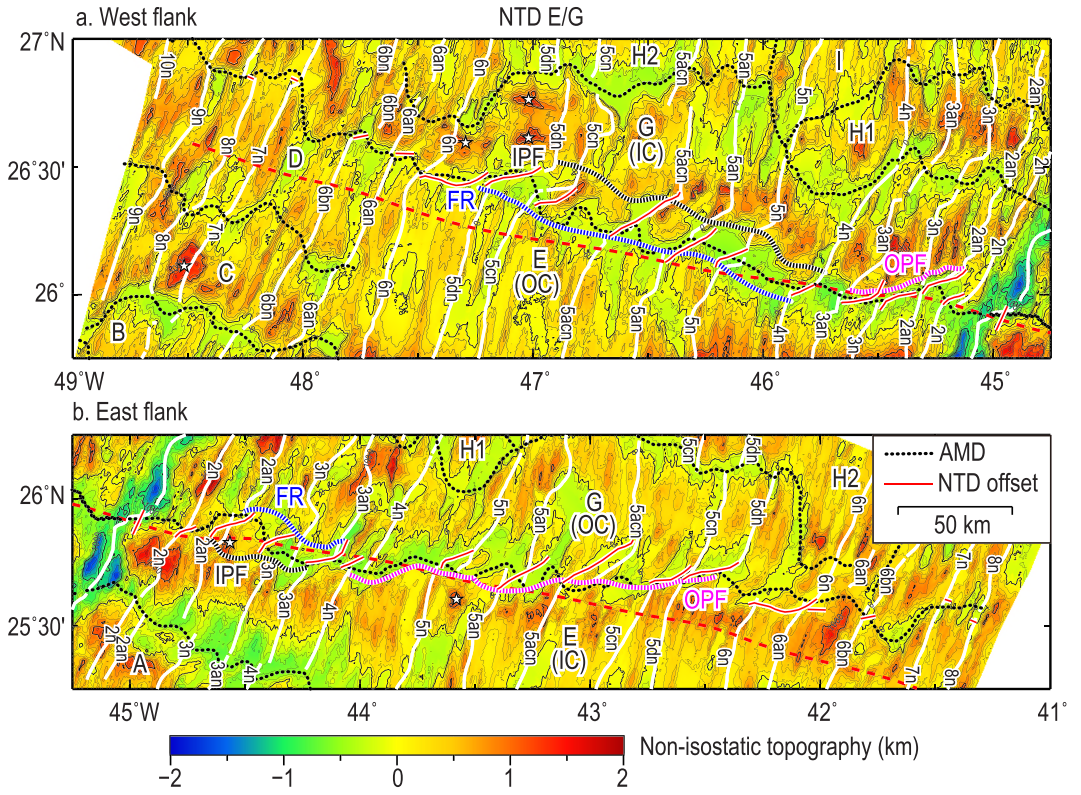

Figure 7. Nonisostatic topography of nontransform discontinuity (NTD) E/G on (a) the west flank and (b) the east flank of the Mid-Atlantic Ridge (MAR). Contour interval is 200 m. The NTD propagated southward between Chrons 5dn and 4n, and northward between Chrons 3an and 2an. IC and OC labels apply from about Chron 7n to present. NTD offsets (red) are from reconstructions in Figures S36 to S51. Explanation is as in Figure 6.

The AMD of the NTD at the southern margin of segment A is the northern limit of a ~60-km-long oblique section of the MAR rift valley that is divided into a series of at least four short spreading segments with intervening small offsets. Off-axis these segments tend to exhibit isolated volcanic edifices and other highly irregular topography rather than continuous abyssal hills, and they also have elevated RMBA (i.e., thin crust; Figure 1b; Zonenshain et al., 1989). This region is considered to be a major transitional shear zone (Rona & Gray, 1980).

4.4. NTD A/E

4.4.1. Structure

NTD A/E is the most consistently propagating discontinuity within our study area (Figure 1c and Table 2). It has always had a right-lateral offset. The discontinuity initially migrated north and south with offset increasing from near zero to ~20 km until segments B, C, and D merged to form segment E and the offset increased to ~37 km. Since about Chron 5dn (17 Ma) the NTD has propagated northward at an average rate of ~3.5 km/Myr and the offset has decreased to ~5 km at the present MAR axis (Figure 4). Detailed plate reconstructions of this NTD are shown in Figures S20 to S35.

IC crust on the west ridge flank is elevated by an average of 600–700 m compared to OC crust south of the NTD (Figures 1a and 6a). RMBA at the western IC is also elevated (up to ~25 mGal) compared to the OC to the south, implying that the IC crust is up to ~2 km thinner. Linear abyssal hills on the IC terminate abruptly southward at the wall of the NTD, which has steep slopes (up to 40°; Figures 2 and 6; see also Figures S20 to S35). North looking sidescan-sonar images show that these steep slopes are locally irregular and strongly reflective, suggesting that mass wasting has kept the slopes free of significant sediment cover. Overall, the IC wall is relatively linear from Chron 6bn to present.

Journal of Geophysical Research: Solid Earth

10.1029/2019JB017648

Table 2
NTD Characteristics, Organized by Propagation Rate

NTD		Approximate chrons	Average age interval (Ma)	Average time (Myr)	Average propagation distance (km)	Propagation rate (km/Myr)[a]	Half spreading rate (km/Myr)	PR/SR	Prop. direction	Offset (km)[b]	IC/OC morphology, propagating segment[c]	IC/OC morphology, doomed segment[c]	IC/OC RMBA of propagating segment[c]	IC/OC RMBA of doomed segment[c]	Pseudofault structure[d]
a. Fast propagation	G/H P1	6n-5dn	18.9–18.4	0.5	33.2	66.3	25	265%	North	0 increasing to ~10 LL	Developing, OCC in prop. ridge tip	Developing	Yes	No	No
	D/G P1	7n	24.1–23.2	0.9	39.8	44.2 (-)	18.5	239%	South	1 increasing to ~5 RL	No	No	Yes	No	No
	G/H P3	5n	11.6–9.4	2.2	45.1	20.5 (-)	16.5	124%	South	0	Yes	No	Yes	No	No
	G/H P4	4n	8.8–7.2	1.6	28.2	17.6	13	135%	North	0 increasing to ~5 RL	Developing	Yes	Yes	No	No
	H/I P1	5n-4n	10.2–8.1	2.1	35.3	16.8	15	112%	North	0 Later change to ~5 LL	Developing	Developing	Initially, then no	Yes	No
b. Slow propagation	D/G P2	6bn	23.2–21.4	1.8	14	7.8	12.7	61%	North	~2–5 RL	Yes	Yes	No	Yes	No
	E/G P3	2an -1n	3.1–0	3.1	17.4	5.6 (-)	13	43%	South	~5–15 RL	Yes	Yes	No[e]	Yes	Yes
	G/H P2	5cn-5acn	15.8–12.8	3	15.6	5.2	14.5	36%	North	~10 LL reducing to ~0	Yes	Yes	Yes	No	No
	E/G P2	3n-2an	6.0–3.1	2.9	14.5	5.0	11.5	43%	North	10–12 RL	Yes, OCC	Yes	Yes	No	Yes
	H/I P2	3an-1n	6.4–0	6.4	28.8	4.5 (-)	12.5	36%	South	~3 LL through zero to ~3 RL	OCC. Yes. LL pattern persists to <2n	Yes, develops after 2an	Yes, but LL RMBA persists to 1n[e]	Yes, develops after 2an	No
	G/H P5	2an-1n	3.2–0	3.2	14.1	4.4 (-)	12.8	34%	South	~5 RL	No	Yes	No[e]	Yes	No
	A/E	5dn-1n	17.4–0	17.4	60.9	3.5	13.7	26%	North	~37 reducing to ~5 RL	Yes	Yes	Yes	Variable[e]	Yes
	E/G P1	5cn-4n	16.7–8.0	8.7	20.9	2.4	14.5	17%	South	~30 to ~9 RL	Yes	Yes	Yes	Yes	Yes
c. No propagation	E/G S1	6bn-5cn	21.4–16.7	4.7	0	0	16.5	0%	None	~8–22 RL	IC/OC morphology both north and south of NTD		IC/OC differentiation north of NTD but not to south		Initating at end of period
	E/G S2	4n-3an	8.0–6	2	0	0	12.9	0%	None	~8–12 RL	IC/OC morphology both north and south of NTD		IC/OC differentiation both north and south of NTD		Transition from S to N propagation

Journal of Geophysical Research: Solid Earth

10.1029/2019JB017648

Table 2
(continued)

NTD	Approximate chrons	Average age interval (Ma)	Average time (Myr)	Average propagation distance (km)	Propagation rate (km/Myr)[a]	Half spreading rate (km/Myr)	PR/SR	Prop. direction	Offset (km)[b]	IC/OC morphology, propagating segment[c]	IC/OC morphology, doomed segment[c]	IC/OC RMBA of propagating segment[c]	IC/OC RMBA of doomed segment[c]	Pseudofault structure[d]
G/H S1	6an-6n	21.1–18.9	2.2	0	0	13	0%	None	0	IC/OC morphology both north and south of NTD; OCC south of NTD		IC/OC differentiation south of NTD but not to north		No
G/H S2	5dn-5cn	18.4–15.8	2.6	0	0	16.8	0%	None	~8–10 LL	IC/OC morphology both north and south of NTD; OCC south of NTD		IC/OC differentiation south of NTD but not to north		No
G/H S3	5an	12.8–11.6	1.2	0	0	16.2	0%	None	~0 LL switching to RL	IC/OC morphology both north and south of NTD		IC/OC differentiation switching from south to north of NTD		No
G/H S4	4n-2an	7.2–3.2	4	0	0	12.7	0%	None	~4–12 RL	IC/OC morphology both north and south of NTD		IC/OC differentiation both north and south of NTD		No
H/I S1	4n-3an	8.1–6.0	2.1	0	0	12	0%	None	~0–3 LL	IC/OC morphology both north and south of NTD		IC/OC differentiation north of NTD but not to south		No
I/J	4an-1n	9.5–0	9.5	0	0	12	0%	None	~0–7 RL	IC/OC morphology both north and south of NTD		IC/OC differentiation both north and south of NTD		No

Abbreviations: IC: inside corner; OC: outside corner; NTD: nontransform discontinuity; RMBA: residual mantle Bouguer anomaly.
[a]Propagation is to the north, except marked by (-), indicating to the south. [b]Average of conjugate ridge flanks; LL, left lateral; RL, right lateral. [c]Exhibits characteristic IC/OC structure and RMBA as described in text. [d]Exhibits identifiable transferred crust (e.g., edifices) between the inner pseudofault and the failed rift. [e]Strong cross-axis asymmetry of RMBA in crust younger than Chron 2an-2n affects the expected IC/OC gravity signature.

OC crust south of the NTD on the west ridge flank exhibits long linear abyssal hills that commonly curve toward the ridge axis where they extend into the NTD. The shallower ridges that are not covered by sediments often extend to within 5 km or less from the northern, IC wall.

On the east flank of the ridge, IC crust is in segment A south of the NTD. As on the west flank, it averages ~600–700 m shallower than OC crust on the north side of the NTD (Figure 6b), and the RMBA is also more positive (up to ~30 mGal) than the OC crust (Figure 1b). Compared to the IC of the west ridge flank, the east-flank IC wall of the NTD is discontinuous and relatively irregular, exhibiting stronger depth variations between alternating highs and lows. The IC wall abutting the topographic highs is generally steep, but in intervening areas, it has more moderate slopes. Linear abyssal hills within segment A are truncated northward at the IC wall.

East-flank OC crust, in segment E north of the NTD, exhibits linear abyssal hills at the margin of the NTD. Unlike OC crust in segment A on the west ridge flank, these ridges rarely curve toward the ridge axis within the NTD. Notable exceptions occur near Chrons 5cn to 5n where septa cross the NTD valley (Figures 2, 6b, and S22–S26).

The eastern NTD valley is much more complex than the western valley because, unlike the western valley, it is interrupted by numerous large, blocky edifices between the southern IC wall and the AMD, and by septa that cross the NTD valley. Most of the edifices are connected only to IC crust on the south side of the NTD (Figure 6b). All the edifices and septa exhibit irregular, lumpy texture and scattered small seamounts on their surface in sidescan-sonar images, suggesting that they are primarily of volcanic origin. The edifices and septa are spaced 5–60 km apart (average ~20 km) over the run of the NTD; thus, at observed spreading rates, they were formed at age intervals of 1–4 Myr (average 2 Myr).

Visually, the "width" of the NTD valley differs significantly between the west and east ridge flanks. As a practical matter, we consider NTD width to be the distance between the average ends of OC abyssal hills (which are mostly curved on the west flank and straight on the east flank) and the IC wall (which is steep and relatively continuous in the west, but in the east is irregular and truncates segment A structure south of the intra-NTD edifices and septa noted above). Measured in this way, the west flank NTD width averages a few kilometers at most, while the east flank width averages 10–20 km.

4.4.2. Application of a Propagating Rift Model

All the features described above are consistent with a propagating rift model (Hey, 1977; Hey et al., 1986) in which the rift axis in segment A has propagated northward with respect to flowlines of relative plate motion (Figure 1). The intermittent occurrence of edifices and septa within the east flank NTD implies that propagation occurred in discrete steps (the "discontinuous propagation" model of Hey et al., 1986), although propagation at some times may have been more continuous. We infer that intermittent magmatic pulses in one or both of the adjacent segments constructed volcanic edifices within the NTD and that northward jumps of the propagating ridge tip followed during intervening less magmatic, more extensional episodes. RMBA is elevated over both the edifices and the adjacent basins, which indicates that the crust of the edifices is thin. Thus, it is likely that the edifices consist largely of sheeted dikes emplaced by dike propagation from the adjacent segment(s), together with overlying volcanics, but without a significant thickness of layer 3 gabbros.

Using the propagating-rift terminology of Hey et al. (1986), we show in Figures 8 and 9 simplified kinematic models of stepwise, northward propagation that relate to the observed structure of NTD A/E. The fact that rift propagation in our study area occurs in slow-spreading crust leads to some differences with the Hey (1977) and Hey et al. (1986) models as generally applied to intermediate- to fast-spreading ridges. First, because propagating ridge tips can abut relatively cold, thick lithosphere at NTDs in slow-spreading crust, we consider that propagation is constrained to the zone of relatively thin crust within an NTD except at the smallest offsets; in this zone the underlying mantle lithosphere is shallow and is likely to be weakened by serpentinization as seawater penetrates through the thin, tectonized crust. Second, unlike the relatively narrow rift at faster spreading ridges, there is active extension within a wide (20–30 km) rift valley at the MAR that can allow for lateral jumps of the ridge axis. However, the zone of active magmatism in the thinnest and weakest lithosphere is only ~5–12 km wide between the first major scarps that bound the inner-valley floor (Smith & Cann, 1993). We refer to this as the "central rift," and we expect that essential tectonic features of the propagating rift model can appear when ridge-axis offsets within NTDs are comparable to or larger than the width of this rift, as at NTD A/E

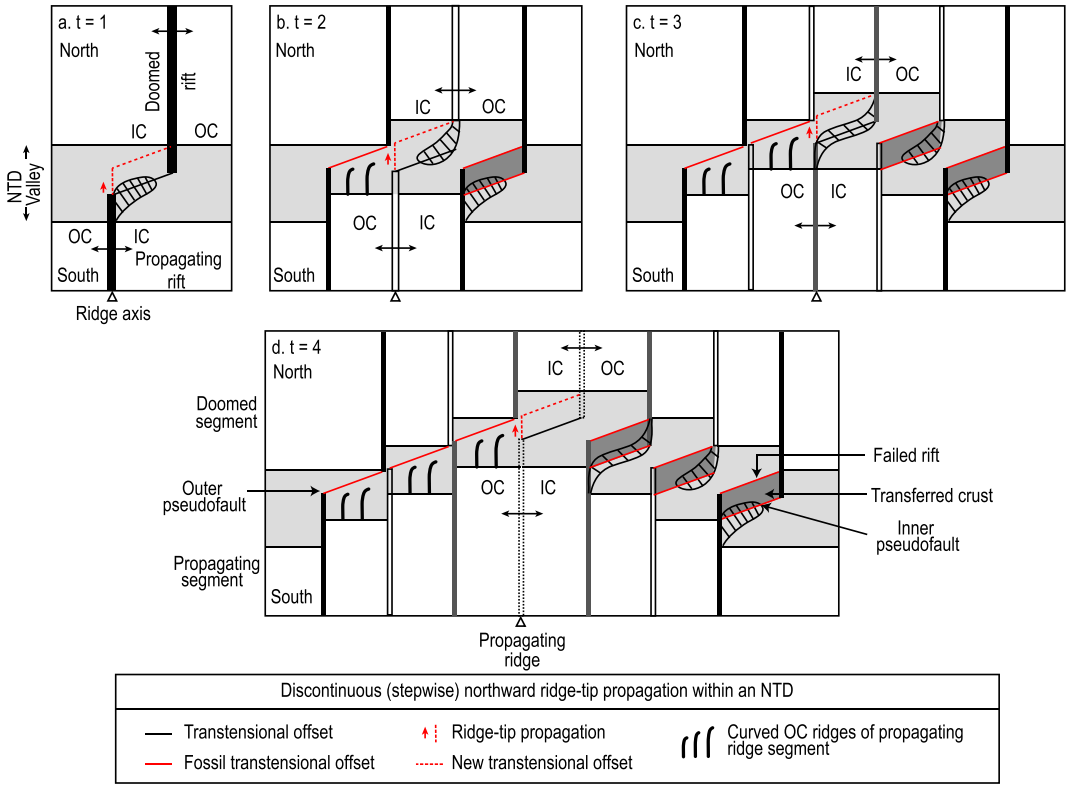

Figure 8. Schematic model of northward propagation of nontransform discontinuity (NTD) A/E and formation of three types of edifices within the NTD. Ridge-axis offset is assumed to be greater than the typical width of the central rift between the first major bounding faults at the sides of the rift axis (~5–10 km). Crust is transferred from one ridge flank to the other only within the NTD valley (shaded). Tectonic elements are labeled in the bottom panel. At time t1 a volcanic edifice that formed at the propagating ridge tip is captured by a northward jump of the ridge tip and is transferred to the eastern NTD valley (time t2). At time t2 an edifice attached to the northern ridge tip is captured by the propagating ridge and transferred, and at time t3 a continuous edifice (septum) across the offset ridge axis is captured and transferred. In all cases the edifices are transferred to the eastern NTD valley. Note that after propagation begins (time t2 and following), the NTD on the east flank is wider than on the west flank. Note also (1) the relatively continuous outer pseudofault, (2) the discontinuous inner pseudofault and failed rift, and (3) the curved abyssal hills on the west flank of the propagator; compare these features to observed structure in Figure 6. Propagation is here depicted as being stepwise but in some cases it may be more continuous.

(Figure 4e). Finally, our models do not require any change in relative plate motion or a mismatch in orientation between the propagating and doomed rift; propagation is in response only to increased extension at the propagating ridge tip, as controlled by reduced magma supply. Despite these differences, our models show all the fundamental morphologic features of a standard propagating-rift model and they appear to explain the observed structure of NTD A/E.

We observe three kinds of edifices in the NTD (Figure 8): (1) attached to the northern segment, (2) attached to the southern segment, or (3) continuous septa across the NTD. The model shows discrete northward jumps of the propagating ridge tip after the edifices are formed. At time $t = 1$ (Figure 8a) magmatism in the southern segment extends northward along the central rift, constructing a volcanic edifice that reaches into the NTD; this is followed by a northward jump of the propagating rift during a succeeding period of low magma supply and thus increased tectonic extension. The edifice is transferred to the east flank between the inner pseudofault (IPF) and the failed rift (FR) in the eastern NTD valley ($t = 2$, Figure 8b). The transferred crust is captured from the northern IC crust only within the NTD valley; we observe no instances where crust was captured from the IC high of the doomed (retreating) segment. Examples of the construction of a volcanic edifice, followed by a northward jump of the propagating ridge tip and crustal transfer, are shown in Figures S21 and S22 for the time of Chron 5dn to 5cn and in Figures S28–S30 for the time of

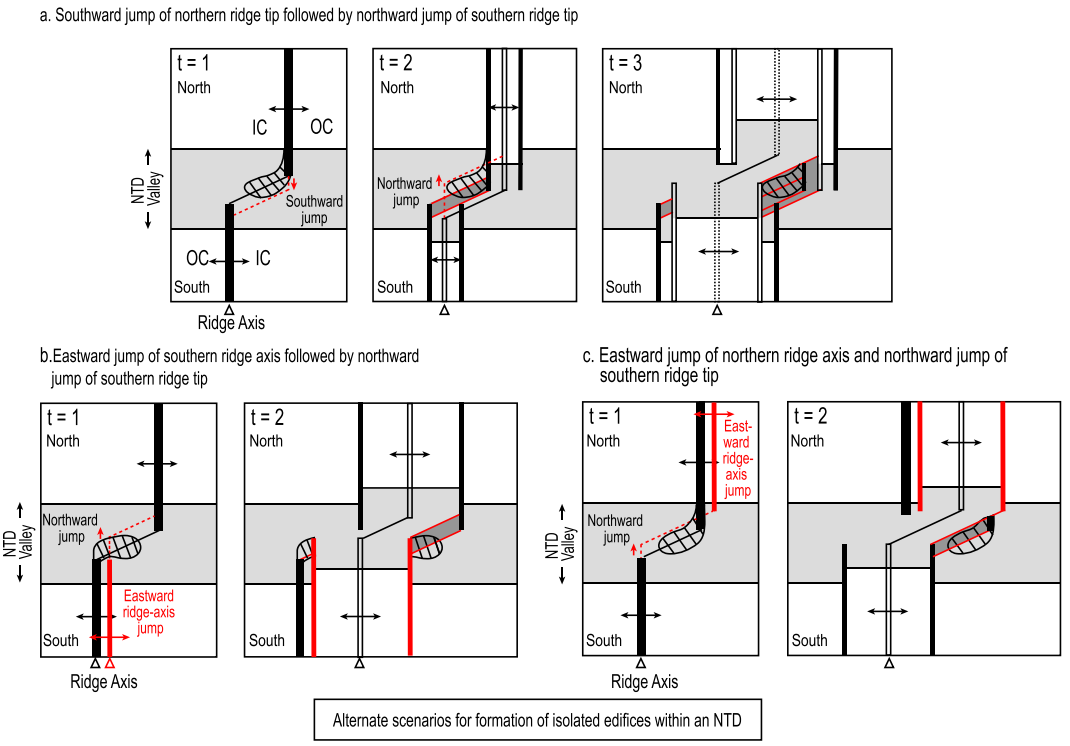

Figure 9. Schematic model showing three possible explanations for the origin of isolated edifices within a nontransform discontinuity (NTD) valley. (a) Southward followed by northward ridge-tip propagation. (b) Eastward jump of the southern ridge axis accompanied by northward propagation of the southern ridge tip. (c) Eastward jump of the northern ridge axis together with northward propagation of the southern ridge tip. See Figure 8 caption for explanation.

Chrons 4n_5n to 3an. The transferred edifices are attached to the IC high of the southern segment and generally show irregular, lumpy topography with volcanic features. We rarely see evidence of a discrete transcurrent fault that connects the offset ridge tips within the NTD. In some places the FR at the northern margin of transferred blocks is relatively linear (e.g., Figure 2a), and this is interpreted to be the position of a transtensional plate boundary at some point during the propagation cycle.

At time $t = 2$ (Figure 8b), magmatism in the central rift of the northern segment constructs a volcanic edifice that extends south into the NTD; this is followed by a northward jump of the propagating ridge tip, and the edifice is captured and transferred to the east flank between the IPF and FR of the NTD valley ($t = 3$; Figure 8c). Again, transferred crust is captured only from within the NTD valley. An example is shown in Figure S32 for a ridge that formed at the southern end of OC crust in segment E between Chrons 3an and 3n prior to a northward jump of the propagating ridge tip at Chron 3n. The transferred crust is attached to segment E along the north side of the NTD.

At time $t = 3$ (Figure 8c), a continuous septum extends across the transtensional plate boundary between ridge tips of the adjacent spreading segments. A northward jump of the propagating ridge tip captures the entire ridge and transfers it to the eastern NTD (Figure 8d). Figure S25 shows an example of a septum that formed just before Chron 5an and was transferred entirely to the east flank by a northward jump of the propagating ridge tip.

In all these cases, crust between the IPF and FR on the east flank of the MAR contains the transferred volcanic edifices together with crust in their adjacent basins. On the east flank, elevated IC crust at the IPF has generally moderate to steep slopes (Figure 6b). The OC at the FR has mostly straight linear ridges that terminate rather abruptly. Some of these ridges may have been truncated by northward jumps of the propagating ridge tip, while others simply could not extend southward against the force of the northward-propagating stress field.

The elevated cold, thick lithosphere of the western IC at the outer pseudofault (OPF) provided a structural and thermal barrier against ridge-tip propagation, represented by the steep southern wall of the IC

(Figure 6a). The OC crust on the south side of the NTD exhibits curvilinear ridges that extend across the NTD, intersecting the steep IC wall at the OPF. This is particularly noteworthy at Chrons 5acn to 5n (Figure 6a). Reduced stress behind the propagating ridge tip allowed the development of curved abyssal hills on the OC, reflecting rotation of the stress field at the ridge tip. As in the propagating rift model of Hey (1977) and Hey et al. (1986) the width of the NTD on the west flank is significantly less than the NTD width between the IPF and the FR on the east flank.

There are rare instances where relatively isolated edifices occur within the NTD on the east ridge flank (e.g., Figures 6b and S27 at Chrons 5acn and 5n). It is unlikely that these were constructed by isolated magmatism in the relatively cold center of the ridge-axis offset, so they probably result from shifts of transtensional faults within the NTD. Figure 9 shows three possible explanations for the isolation of such edifices. In the first case (Figure 9a), the northern segment formed a volcanic edifice within the NTD and its ridge tip jumped southward at time $t = 1$. A subsequent northward jump of the southern ridge tip at time $t = 2$ captured the edifice and transferred it to the east flank ($t = 3$). In the second case (Figure 9b), an edifice connected to the southern segment is isolated within the eastern NTD valley by an eastward jump of the southern ridge axis and a northward jump of its ridge tip. In the third case (Figure 9c), an edifice connected to the northern segment is isolated within the eastern NTD valley by an eastward jump of the northern ridge axis and northward propagation of the southern ridge tip. Such lateral jumps of the ridge axis ideally could be discerned from the pattern of magnetic anomalies. However, abyssal hills and related edifices in the NTD are typically only 5–10 km wide, so they can be isolated within the NTD valley with a ridge jump of half this distance ($\lesssim$5 km). Errors in picking magnetic anomalies in the slow-spreading crust of the MAR can easily equal or exceed these distances (Tivey & Tucholke, 1998; Vogt, 1986), so it is difficult to define exactly where such jumps may have occurred.

4.5. NTD D/G and E/G

This NTD (D/G up until Chron 6an, E/G thereafter; Figure 1) on average has propagated irregularly southward with respect to plate flowlines since Chron 10n (28 Ma). Most of this propagation occurred first during a brief, very rapid episode between Chrons 7n and 6bn (D/G P1; 44.2 km/Myr) and then during a longer period between Chrons 5cn and 4n (E/G P1) when the propagation rate was ~2.4 km/Myr (Figure 1c and Table 2). Propagation direction changed to the north during a short but distinct period just before Chron 6bn (D/G P2) at a rate of ~7.8 km/Myr. Following Chron 3n the NTD also propagated briefly northward at 5 km/Myr, then southward to the present ridge axis (E/G P2 and E/G P3, respectively, in Figure 1c). Detailed features of the NTD are shown in plate reconstructions in Figures S36 to S51.

Prior to Chron 7n, the NTD was moderately stable and had minor ridge-axis offsets less than ~2–3 km that varied between right- and left-lateral (Figures 1c, 7, S36, and S37). At this time there was little difference between adjacent IC and OC crust in terms of depth, RMBA, or structure, except that a domed oceanic core complex (OCC) developed at the western IC between Chrons 9n and 8n. The NTD is defined only by moderate depression of linear abyssal hills and by intervening basins.

Beginning with the brief episode of fast southward propagation following Chron 7n, and continuing to the present, the NTD developed a more typical valley bounded by characteristic IC and OC crust (Figures 1 and 7). Average ridge-axis offset increased to ~20 km from 19 to 9 Ma and subsequently decreased to about 10 km (Figure 4). During a quasi-stable period between Chrons 6bn and 5dn, an irregular OCC developed on the western IC, followed by two, more-linear OCCs within segment G just to the east (Figures 1 and S41).

NTD E/G had a ridge-axis offset of ~20 km during the period of southward propagation between Chrons 5dn and 4n, and its structure is distinctly different from that of the more-stable periods, most notably on the west flank of the MAR (Figure 7a). Interpreted in the context of our propagating rift models, several large edifices along the western IC represent crust between the FR and IPF, transferred from the east ridge flank by southward propagation of the segment G ridge tip. These edifices show irregular structure in sidescan-sonar images, with little indication of linear, ridge-parallel faults or volcanic topography (Figures S42–S46). OC abyssal hills abutting the OPF on the east flank tend to show more curvature where they enter the NTD than do OC abyssal hills at the FR on the west flank, which is consistent with a stress field associated with southward propagation. As was interpreted in the propagating rift of NTD A/E, the width of the NTD valley on the IPF (west) side of the ridge also is greater than on the OPF (east) side.

There are two principal differences between the structure of the propagating rift at Chrons 5dn to 4n in NTD E/G and the structure NTD A/E. First, the trace of the OPF along the IC in NTD E/G is somewhat more irregular and has overall lower slopes than that of the OPF in NTD A/E (compare Figures 6a and 7b). Second, unlike NTD A/E where edifices and septa are observed within the NTD valley only on the IPF side, NTD E/G has these structures on both ridge flanks. Most notable are a septum and an isolated edifice between Chrons 5n and 5acn along the OPF on the east ridge flank (Figures 7b, S44, and S45). We attribute these differences to the slower and perhaps more continuous propagation of NTD E/G (2.4 km/Myr) compared to NTD A/E (3.5 km/Myr); this may have allowed septa to develop at the ridge axis and then be rafted to the east ridge flank without rapid southward propagation of the ridge tip capturing the septum and transferring it to the IPF in the western NTD.

In contrast, the short period between Chrons 3an and 2an during which NTD E/G propagated more rapidly northward shows structure that is very similar to that of NTD A/E (Figures 7 and S49–S51). The ridge-axis offset was ~12–14 km and the IC at the OPF on the west flank has a steep and continuous wall, while abyssal hills in the OC to the south curve into the offset and approach the IC wall. OC abyssal hills abutting the FR on the east flank are linear, while blocky edifices (including a poorly developed OCC) are present between the FR and IPF. Since Chron ~2an the offset again readjusted but has maintained an ~8- to 10-km offset; it stepped south while a major edifice developed at the northern IC, similar to the edifices south of the IPF during the earlier phase of southward propagation between Chrons 5dn and 4n.

4.6. NTD G/H

NTD G/H has had a complex evolution that was affected by very fast propagation, quasi-stable periods, temporary merger with NTD H/I, and formation of well-developed OCCs in segment G (Figure 1). Throughout its history, ridge-axis offsets in the NTD have been ~10 km or less (Figure 4), that is, comparable to the width of the central rift. The NTD is referred to as G/H1 after its temporary disappearance around Chron 5n and as G/H2 before that time. The NTD appears to have originated between Chrons 6bn and 6an, although it showed little clear offset or topographic expression until after Chron 6n (Figures S52–S55). Consequently, no characteristic patterns of IC vs. OC crustal structure or RMBA were developed. There is a very strong difference (~15–25 mGal) in average RMBA between west- and east-flank crust in plate reconstructions but no significant difference in gross crustal morphology (e.g., Figure S52). Thus, it seems unlikely that the RMBA differences reflect effects from the shallow lithosphere (e.g., crustal thickness and tectonic extension), and we attribute them to density differences in the deeper mantle (see section 5.4).

During a period of near-zero offset shortly following Chron 6n, NTD G/H2 propagated very quickly (within 0.5 Myr) ~33 km northward to a position on the north side of a well developed OCC within segment G (G/H P1), and clear IC/OC differences in morphology and RMBA began to appear (Figures 1 and S55, and Table 2). Preferential crustal emplacement at the OCC resulted in asymmetric spreading and created a left-lateral, 10- to 20-km offset in the NTD that continued until about Chron 5an (Figures 4 and S56–S58). During the first part of this period, the NTD was relatively stable (Figure 1c), but it then propagated northward from Chron 5cn to 5an (G/H P2) and its offset diminished to zero (Figures 4, S57, and S58). IC/OC structural characteristics were well developed throughout this period. RMBA in IC crust south of the NTD was elevated by 8–24 mGal compared to OC crust on the north side, although there was little difference between conjugate IC and OC crust on the north side.

NTDs G/H2 and H2/I temporarily merged between Chrons 5an and 5n, forming NTD G/I until the discontinuity again split into NTDs G/H1 and H1/I (Figure 1). During this period and up until ~9 Ma, following Chron 5n, NTD G/I and then G/H1 propagated very rapidly southward at a rate of ~20.5 km/Myr (G/H P3; Figures 1c, S59, and S60) and then briefly northward at ~17.6 km/Myr until slightly after Chron 4n (G/H P4; Figure S61). There was little to no offset in the NTD during these propagations and consequently no distinctive IC/OC structure, but by Chron 4n to 3an a right-lateral offset was established. The RMBA reflects the transition from IC/OC structure characteristic of a left-lateral offset prior to Chron 5an (even though there was little or no offset at that time) to structure characteristic of right-lateral offset following Chron 4n; specifically, the pattern of elevated RMBA to the southwest and northeast of the ridge-NTD intersection (Figures S57 and S58) shifted to elevated RMBA at ICs to the northwest and southeast of the intersection (Figures S60 and S61).

Following Chron 4n up to Chron 2an, NTD G/H2 had a right-lateral offset, typically ~10 km (Figures 1, 4, and S60–S63). During that time, the NTD was quasi-stable, and it mostly shows somewhat irregular, high IC massifs with elevated RMBA and deeper, more lineated OC abyssal hills with lower RMBA. Inward-facing normal faults bounding abyssal hills on both IC and OC crust commonly curve into the offset.

The NTD has propagated slowly southward since Chron 2an. The offset became smaller at Chron 2n but subsequently increased to ~8 km at the present ridge axis. The typical IC/OC structure and RMBA patterns disappeared, and there is no clear structure characteristic of a propagating rift. Both IC and OC crust on the east ridge flank are dominated by large, irregular faults and elevated RMBA, while the west-flank IC and OC crust both have lineated abyssal hills and RMBA up to 20–25 mGal lower. This difference has been interpreted to be a result of strong asymmetry in tectonic extension on the two ridge flanks (Wang et al., 2015).

Except during the periods of very fast propagation when there was little or no offset and NTD width thus is difficult to define, the width of NTD G/H averaged about 10 km on both ridge flanks. Significant septa developed across the entire NTD at several times when it had offsets of a few kilometers to ~10 km and was propagating slowly northward (e.g., Chron 5acn; Figure S57) or was quasi-stable (Chron 5an, Figure S58, and Chrons 3an and 3n, Figures S61 and S62). The septa usually exhibit small-throw normal faults associated with abyssal hills that curve across the NTD, together with minor irregular faults and occasional volcanic cones. They show no indication of strike-slip faults orthogonal to the spreading direction. They occur randomly on both sides of the MAR, and thus, there was no systematic transfer of crust from one ridge flank to the other as would be expected in a propagating rift.

4.7. NTD H1/I

NTD H1/I formed following Chron 5n and has had only small ridge-axis offsets of ~5 km or less throughout its history (Figure 4). It separated from the temporary G/I discontinuity and propagated rapidly northward (H/I P1) at an average ~16.8 km/Myr in the presence of zero offset until Chron 4n (Figures 1c, 4, and S66, and Table 2). It subsequently developed a small left-lateral offset of ~5 km and was quasi-stable to approximately Chron 3an, then shifted to zero offset and propagated slowly southward (H/I P2) at about 4.5 km/Myr; it only recently developed an ~5-km right-lateral offset at the present ridge axis (Figures S66–S71). Throughout its evolution, even during the time when it had observable offset, the NTD has been crossed by abyssal hills (septa). Its position is defined largely by saddles in the abyssal hills, by adjacent basins, and particularly by RMBA patterns. RMBA at the IC northeast of the NTD was elevated relative to OC crust even before the NTD developed its left-lateral offset near Chron 3an (Figures S66 and S67), and it continued to be elevated until Chron 2an, while the NTD offset was near zero (Figures S68–S70). Elevated RMBA at the southwest IC developed gradually over the same period. There is a clear correspondence between the occurrence of larger-throw, more irregular faults (i.e., increased extension) and elevated RMBA at IC positions, particularly the northern IC, throughout the development of the NTD (Figures S67d and S67e to S69d and S69e). The strong extension indicated by elevated RMBA and faults at the northern IC may have driven the southward propagation from about Chron 3an to the present. A well-developed OCC formed just north of the NTD following Chron 2n (Figure S71; Tucholke et al., 2001). There are no distinct features of the NTD (e.g., pseudofault structure or different widths on the two ridge flanks) that would be expected in a propagating rift.

As in segment G since about Chron 2an, the RMBA on the east flank of the MAR, both north and south of the NTD, has been significantly higher than on the west flank (Figures S70 and S71); this has been attributed to asymmetric faulting in the rift valley (Wang et al., 2015).

4.8. NTD I/J

NTD I/J is the most stable discontinuity within our study area. It has departed from flowlines of relative plate motion by no more than a few kilometers since Chron 4an and over that period has had a small right-lateral offset averaging ~5 km (Figures 4 and S72–S77). No long-range sidescan-sonar data are available in this part of the survey area, but multibeam bathymetry clearly show typical IC/OC morphological characteristics, that is, elevated, irregular IC crust compared with deeper OC crust exhibiting linear abyssal hills, many of which curve gently into the offset on both flanks of the MAR. This IC/OC differentiation is also well represented in the RMBA, with IC crust averaging 8 to 26 mGal higher than OC crust.

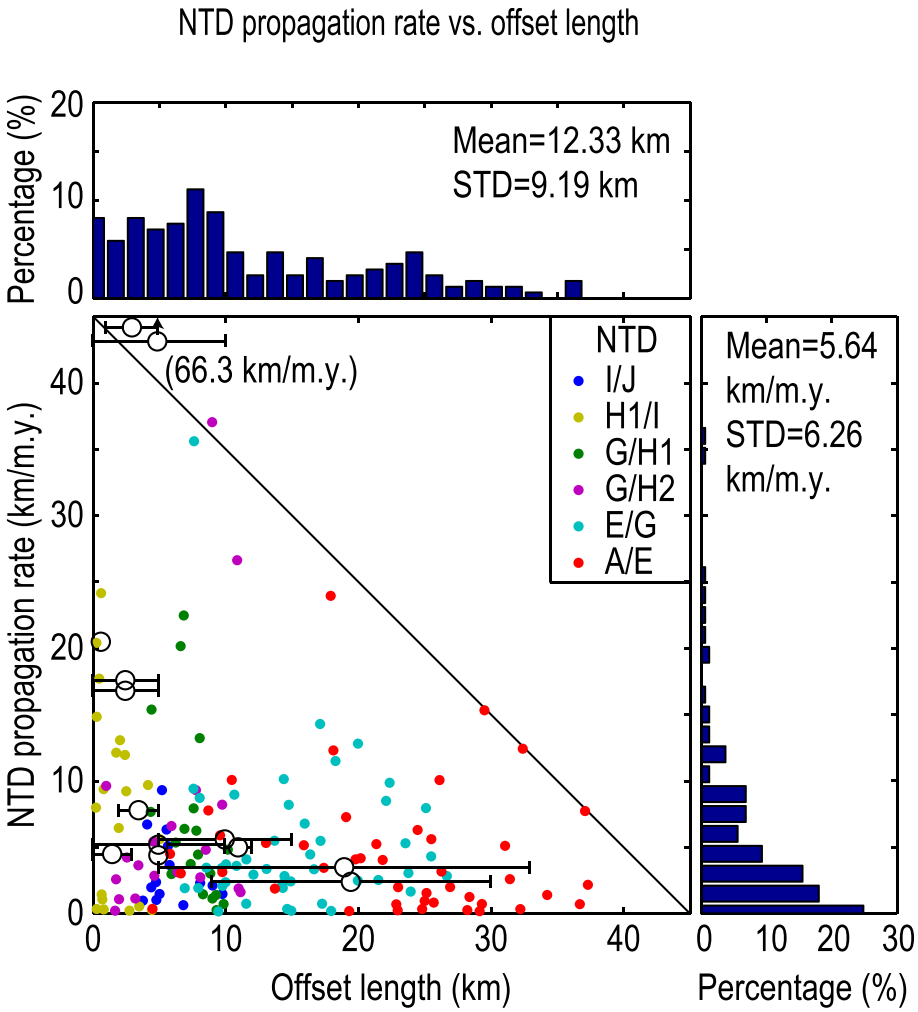

Figure 10. Nontransform discontinuity (NTD) propagation rate versus offset length, averaged for conjugate ridge flanks. Small dots show short-term propagation rates calculated from AMD positions at 0.5-Myr intervals; these events occurred mostly within the width of the NTD at the ridge axis. The large circles show rates for long-term propagation (Figure 1c) together with the associated range of offsets; see Table 2.b for NTD identifications. Large offsets ($\gtrsim$10 km, i.e., the typical width of the central rift between the first major bounding faults at the sides of the rift axis) do not permit high NTD propagation rates; NTDs may or may not propagate quickly when offset lengths and time intervals are small. Propagation rates rarely exceed ~10 km/Myr irrespective of offset. Plots of point frequency at top and right are for short-term propagation.

5. Discussion

5.1. Scales of NTD Propagation

NTDs in the study area have migrated along the MAR axis at two different time and length scales. At short scales, and taking their AMDs as a guide, all NTDs propagate north and south along the ridge axis at time scales less than ~1 Myr and length scales less than ~10–15 km (Figure 1). These small-scale propagations can occur very rapidly (Figure 10), and they give the NTDs a markedly irregular appearance off-axis. With propagation distances less than ~10–15 km, they occur within the average widths of the NTDs (~8–25 km), and thus, they appear to represent random repositioning of the transtensional plate boundary between ridge tips of the adjacent spreading segments; in some instances it is possible that they are related to minor changes in the direction of relative plate motion. Such short-term propagation was noted by Spencer et al. (1997), who described septa that cross the offset between ridge tips of adjacent spreading segments at the present MAR axis. They noted that these septa eventually must be carried off-axis, and this is likely accomplished by intermittent propagation and retreat of the transtensional plate boundary within the NTD; this captures the septa and translates them onto the ridge flank.

We differentiate this short-term irregularity from true NTD propagation that occurs at larger scales, that is, at periods ≳1 Myr and/or length scales ≳15 km, as summarized in Figure 1c and Table 2. The random directions of these propagators compared to flowlines of relative plate motion (Figure 1c) clearly show that they are not explained by minor changes in relative plate motion. The fastest observed propagation (~16.8 to 66.3 km/Myr) is about 1.1 to 2.6 times the half spreading rate, and it occurs when NTDs have small to zero offset (Figure 10 and Table 2.a). In these instances depressed abyssal hills commonly cross the discontinuity and pseudofault structure characteristic of a propagating rift is absent. ICs tend to be more elevated than OCs but there is little structural difference between the two. However, RMBA at the IC of a propagating rift is significantly elevated compared to that of the doomed rift, where RMBA values of both the IC and OC are lower (e.g., Figures S56–S59).

Propagation rates of these NTDs are similar to rates of the short-term propagators that give NTDs their irregular appearance, but they occur over much longer length scales of tens of kilometers. In rate and distance, they resemble a pair of small-offset, fast-propagating rifts described by Kleinrock et al. (1997) within our study area. Those propagators crossed the full width of spreading segment E 10–15 Myr ago, and similar possible fast propagators may also have crossed other segments in the study area (Kleinrock et al., 1997). Kleinrock et al. (1997) evaluated mechanisms that might explain the fast propagation and they concluded that the only viable explanation was a reduction in magma supply, represented by an increase in RMBA associated with the propagating rift. With reduced magma supply, increased tectonic extension stimulates crack propagation. This model is consistent with our observation that RMBA is more positive in the propagating rifts (i.e., the crust is thinner due to tectonic extension) than in the doomed rifts.

NTDs that have propagated at rates less than the half spreading rate differ from the fast-propagating discontinuities in several respects (Table 2.b). They have had mostly larger offsets ranging up to ~37 km, and they more consistently exhibit well-developed IC/OC differences of depth and structure in both the propagating and doomed rifts. Similarly, significant IC/OC differences in RMBA are usually developed in both the propagating and doomed rifts, whereas such differences are rare in the doomed rifts of fast propagators.

5.2. Propagation in Relation to Offset

The association of elevated RMBA with propagating rifts, particularly those that are fast propagating, suggests that a primary driving force for longer-term NTD propagation is reduced magma supply at the end of a spreading segment, which results in increased tectonic extension and thus rift propagation into the adjacent spreading segment. However, the rate of propagation is influenced by the magnitude of an offset in an NTD. Where there is a significant offset (≳5-10 km, i.e., greater than the width of the central rift), propagation is hindered because the propagating ridge tip abuts older and colder lithosphere in the doomed spreading segment (E/G P2, A/E, and E/G P1 in Figure 10 and Table 2.b). In these cases typical IC/OC morphology and RMBA patterns develop in both the propagating segment and the doomed segment, and characteristic pseudofault structure is present.

At small to zero offsets (i.e., comparable to the width of the central rift), propagation can occur very rapidly, provided that a zone of reduced magma supply is present in the propagating rift (Figure 10 and Table 2.a). However, the presence of a small offset does not guarantee that propagation will occur quickly (Table 2.b) or at all (Table 2.c). In these latter instances there does not appear to be a consistent correlation between propagation and the presence of IC/OC morphologic or RMBA differences between the two sides of an NTD. This suggests that factors other than just low magma supply (and thus increased extension) can play a role in driving NTD propagation.

5.3. Magma Supply and Its Effect on NTD Evolution

It is commonly assumed that differences in gross magma supply between adjacent segments explain NTD propagation, with the segment that has higher magma supply driving a ridge tip into the segment with lower magma supply (e.g., Brozena & White, 1990; Dannowski et al., 2018; Hey et al., 1980; Hey et al., 1986; Hey et al., 2010). To evaluate this possibility in our study area, we examined differences in magma supply between adjacent segments in two ways, both of which characterize the magma supply within a segment along its length through time. First, we used the magmatic component of extension, M, which is the difference between the tectonic component T (derived from fault throw) and the full extension rate. Note that derived absolute values of T, and thus of M, depend entirely on the dip-limit of fault slopes that we specify; however,

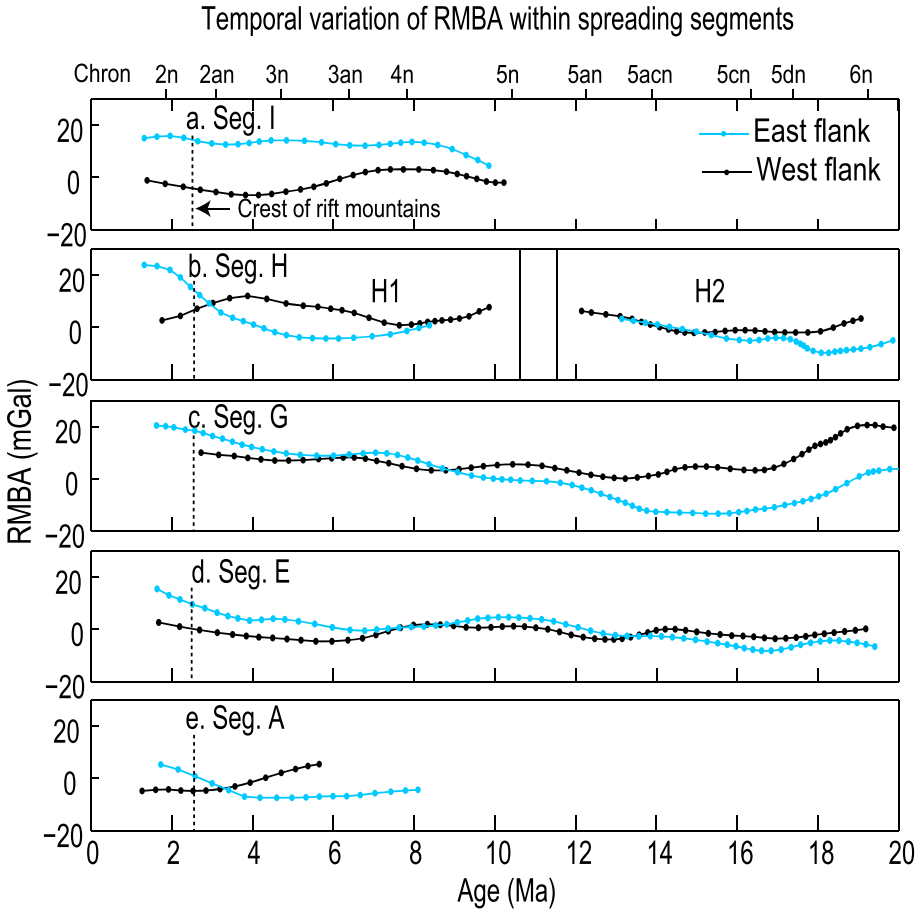

Figure 11. Residual mantle Bouguer anomaly (RMBA) versus age for conjugate ridge flanks in spreading segments A through I. Each point is an average value within a 20-km wide box, as shown in Figure S78, with box steps of 4 km (80% overlap). See text for explanation.

the information of interest in our analysis is the *relative* difference between adjacent segments, so knowing absolute values is not necessary. Second, we used RMBA to determine differences in magma supply between adjacent segments based on the assumption that variations in RMBA primarily reflect changes in crustal thickness, with reduced RMBA corresponding to increased crustal thickness. We examined RMBA over both the full length of segments (i.e., between the bounding AMDs) and within the shorter boxes used to calculate T and M (see section 3.4) and found no significant differences; we use the latter values here. Below, we first examine temporal variations in M and RMBA, and then we evaluate how these may relate to NTD propagation and to segment length.

5.3.1. Temporal Variations in M and RMBA

M on the conjugate ridge flanks of each spreading segment is shown in Figure 3. Long-term trends suggest relatively constant magma supply in segments through time except in segment G, where M has decreased about 8%, and in segment H where M decreased several percent between H1 and H2. M appears to decrease (T increases) sharply within about 2.5 Myr of the ridge axis, which reflects tectonic extension and uplift of crust from the rift valley to the crest of the rift mountains. On the ridge flanks, M fluctuates on time scales of ~1-2 Myr, and it also varies independently between the crustal conjugates. The latter reflects asymmetric distribution of normal faulting at the ridge axis.

RMBA shows patterns that are grossly similar to those of M, although the signal is naturally smoothed in comparison (Figure 11). In particular, RMBA increases (crustal thickness decreases) through time in segment G, there is a small step in segment H from H1 to H2, and it is essentially constant in the other segments. Variations at wavelengths ~3–4 Myr are not in phase on conjugate ridge flanks, and they

probably reflect smoothed, long-term patterns of asymmetric faulting that occurred at the ridge axis. However, there are significant longer-wavelength differences (up to ~20 mGal) in RMBA on conjugate ridge flanks in crust younger than ~8 Ma in most segments and in crust older than about 13 Ma in segment G. These are interpreted to reflect deeper mantle effects, as discussed in section 5.4. In both RMBA and M, the patterns of apparent magma input at the ridge axis through time have been independent from segment to segment.

5.3.2. Relation of M and RMBA to NTD Propagation

If the gross volume of magma supply in a segment relative to its neighbors controls propagation of its bounding NTDs, we would expect NTD E/G to propagate northward with time, given that segment G has had decreasing average magma supply at least since ~14 Ma, while segment E has had a relatively constant supply (Figures 3 and 11). As shown in Figure 1, this is not the case because the NTD propagated southward during most of this period.

Looking more broadly, Figures 12a and 12b summarize propagation rate versus difference in RMBA (interpreted as magma supply) between adjacent segments for all NTDs in the study area. NTD A/E mostly falls just within the lower right quadrant of Figure 12a, which is consistent with slow northward propagation (Table 2) and slightly lower average RMBA (i.e., thicker crust and greater magma supply) in segment A south of the NTD (Figure 11). Unfortunately, these data are limited to the period between 5.8 and 1.2 Ma. Longer-term trends in combined survey- and satellite-derived gravity, however, also suggest that RMBA has decreased with time in segment A, while it has increased in segment E (Figure 1b), consistent with northward propagation being driven by increasing magma supply in segment A. Data for all the other NTDs are widely scattered, indicating that the relative difference in gross magma supply between adjacent segments has little or no effect on propagation. Figure 12c, based on M rather than RMBA, shows the same scattered pattern. Furthermore, propagation rate is not correlated with NTD offset, as shown by the color-coded points in Figures 12b and 12c. Thus, the gross volume of magma supply may play a limited role in NTD propagation as suggested for NTD A/E, but it does not appear to be the primary driving force for propagation within our study area.

5.3.3. Relation of Segment Length to M and RMBA

Change in the length of a spreading segment is the integrated result of ridge propagation or retreat at the two ends of the segment. We might expect that increasing melt supply within a segment would result in increased segment length; that is, it would drive propagation of NTDs at one or both ends of a segment. In Figure 13 we plot the relationship of segment length to magma supply interpreted from M and from RMBA. Note that segment length (Figure 5) can differ by up to ~20 km between the conjugate ridge flanks. This is because we calculated lengths between AMDs, which can differ from the actual offset plate boundary. Short-term propagation within the average width of the NTD valley (up to 25 km) can create significant apparent differences in segment length on conjugate ridge flanks.

The plot in Figure 13 shows considerable scatter, but there appears to be a slight positive correlation between M and segment length (Figure 13a) and a stronger positive correlation between decreasing RMBA and segment length (Figure 13b) if we consider all segments together. However, this differs significantly in individual segments. For example, segment A shows a slight but clear negative correlation. Only in segment E does increasing segment length show some correlation with increasing M and decreasing RMBA. Data for most other individual segments are randomly scattered. Just as there is only a weak correlation of RMBA or M to segment length, there appears to be only a weak possible correlation between RMBA and M (Figure 13c). From these results we expect no significant correlation between segment length and NTD propagation.

5.3.4. 3-D Model of NTD Propagation

Our analyses suggest that with the possible exception of segment A (Figure 12a), gross volume of magma supply within a spreading segment is not a significant driving force of NTD propagation within our study area. On the other hand, Dannowski et al. (2011) provided strong evidence that a large magma flux in the TAMMAR segment south of Kane Fracture Zone was responsible for southward propagation of the discontinuity at the southern end of that segment, even though the offset in the discontinuity was large (40 km).

It is possible to reconcile these differences if there is a threshold value of difference in magma supply between adjacent segments that determines whether a discontinuity will or will not propagate. The seismic studies of

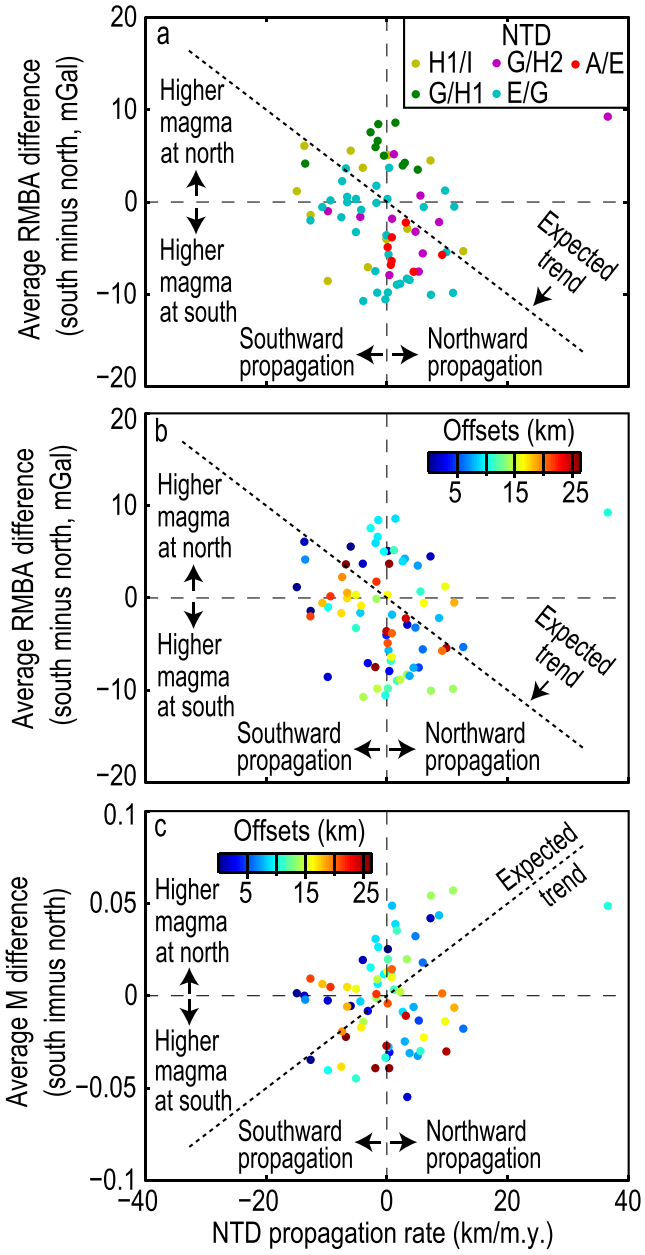

Figure 12. Inferred gross volume of magma supply within adjacent spreading segments versus propagation rate of the intervening nontransform discontinuities (NTDs) within the study area, based on averages of residual mantle Bouguer anomaly (RMBA) and M on conjugate ridge flanks. More negative RMBA indicates greater crustal thickness and thus magma supply. Points are southern minus northern segment values, calculated at 0.5-Myr intervals along flowlines. (a) RMBA difference between adjacent spreading segments versus NTD propagation rate, color-coded by segment. Positive RMBA differences indicate greater magma supply in the northern segment and negative differences indicate greater magma supply in the southern segment. (b) As in (a) but color-coded by magnitude of offset in the NTD. (c) Difference in M between adjacent spreading segments versus NTD propagation rate, color-coded by magnitude of offset in the NTD. Positive differences in M indicate that there is greater magma supply in the southern segment and negative differences indicate greater magma supply in the northern segment. If the gross volume of magma supply within a spreading segment compared to an adjacent segment was the driving force for NTD propagation, points should fall along the trends shown by the dotted lines in the plots.

Dannowski et al. (2011) showed that there was a very large, ~3-km difference in crustal thickness between the center of the TAMMAR segment versus the southern margin of the segment and the adjacent segment to the south. In contrast, the largest difference in crustal thickness between segments in our study area is

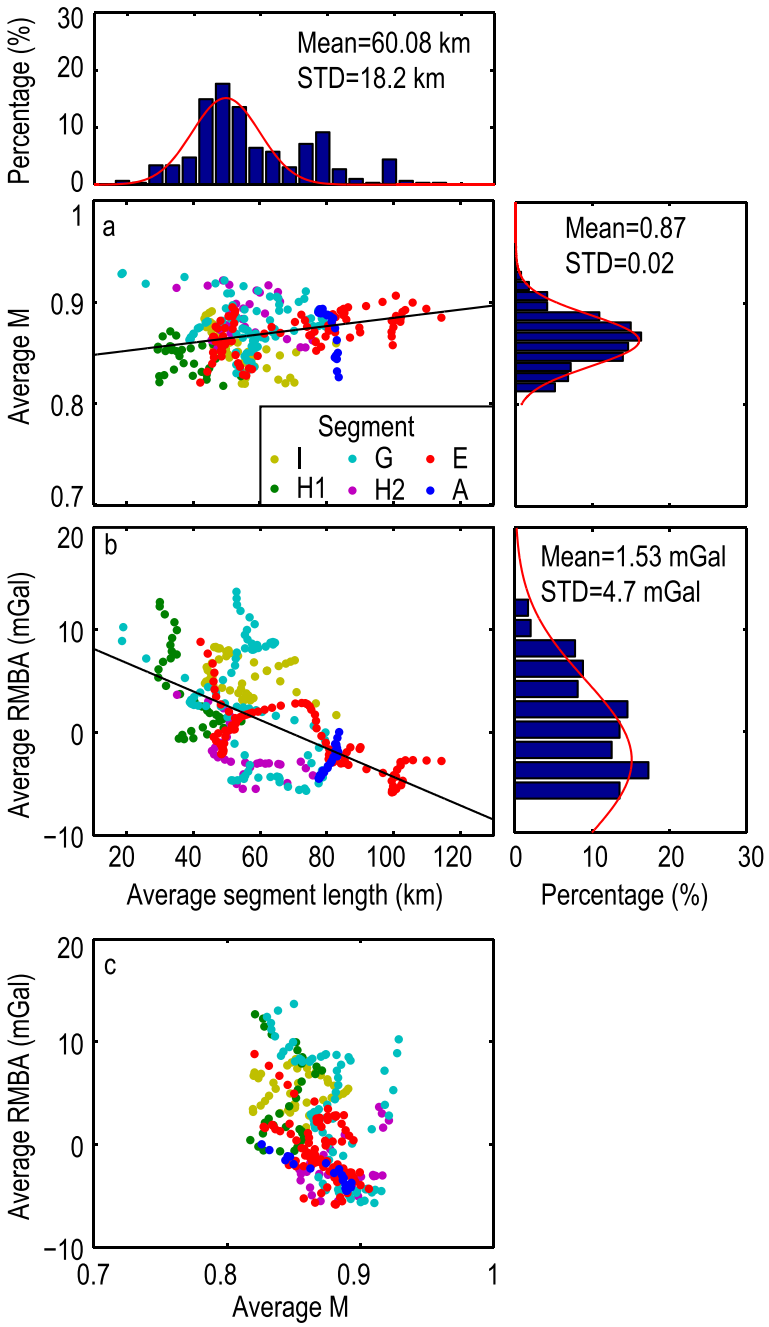

Figure 13. Relationships between M, residual mantle Bouguer anomaly (RMBA), and segment length based on averages of conjugate ridge flanks. Point values are plotted at 0.2-Myr age intervals and are color coded by segment. (a) M versus segment length. (b) RMBA versus segment length. (c) RMBA versus M. See text for discussion. Frequency plots of data points are shown at top and right of (a) and (b).

about 0.9 km, inferred from maximum differences of ~12 mGal in RMBA (Figure 12). These differences are small compared to those at the TAMMAR segment, and we suggest that the differences in our study area are not large enough to drive propagation to any significant extent.

In the case of NTD A/E, however, the NTD consistently propagated northward even though the difference in magma supply between segments A and E was small (maximum difference ~8 mGal, or ~0.6 km in crustal thickness; Figure 12), while other NTDs with comparable or larger differences did not propagate in the expected directions. We suggest that a second factor may have played a role in the northward propagation

of NTD A/E, that is, the way that magma was distributed within segment A. If we compare the average RMBA of the two ridge flanks at the northern margin of segment A with the average of the ridge flanks at the southern margin of segment E (Figure 1b), it is evident that the northern margin of segment A has higher average RMBA values, and the higher values are more widespread. We interpret this to mean that the northern part of segment A had reduced magma supply compared to segment E to the north (even though the gross magma supply in segment A was slightly greater than in segment E), and it therefore experienced greater extension that helped to drive northward propagation into segment E.

The kind of plumbing system that can localize magma deposition within a spreading segment as noted above has been demonstrated in seismic experiments (Magde et al., 2000). Magde et al. showed that rising magma beneath a spreading segment on the MAR at 35°N is constrained to pipe-like features near the base of the brittle lithosphere and then spreads out along-axis at shallower levels to build the crust. If such feeder pipe(s) are not centered in the segment, then along-axis asymmetry in crustal thickness could easily develop. We suggest that such irregular distribution of magma in the lithosphere, which at least partially reflects its distribution in the rising mantle, may be a widespread phenomenon within our study area. The resulting spatial distribution of magmatic and magma-poor (extensional) zones within spreading segments, observed as RMBA lows and highs, respectively, is thus a strong determinant of the evolution of segments and intervening NTDs, and it may also be responsible for their initiation or demise. A good example is shown in Figures S57b–S59b where the spatial migration of a reduced-magma, extensional zone caused a reversal in the propagation direction of NTD G/H, a reversal in offset direction, and the temporary demise of segment H. The general variability of magmatic and extensional zones around NTDs through time can be observed by scanning through the plate reconstructions of RMBA in the figures in the supporting information and by viewing the movies in the supporting information.

There may be a third, related factor that contributed to propagation of NTD A/E, namely, the shifting locus of regions of fertile mantle that melted to supply magma to segment A through time. If these regions were progressively farther north with depth in the mantle, then the northward shifting position of magma delivery from the rising mantle would help to drive propagation. Similarly, the propagation might be assisted by a northward shift in the position of dynamic upwelling.

Putting all these observations together, we suggest that NTD development is the result of a three-tier process. The first, fundamental control is the size and distribution of heterogeneities in the underlying asthenosphere. The heterogeneities may be created by changes in mantle composition, by dynamic instabilities (e.g., Lin et al., 1990; Lin & Phipps Morgan, 1992), or by interplay of the two. These heterogeneities cause the location and gross volume of magma supply beneath the ridge axis to be strongly three-dimensional. Segmentation of the MOR is primarily determined by this asthenospheric control. Secondly, the distribution of magma that is supplied from the asthenosphere to build the oceanic crust within each spreading segment is controlled by the configuration of the lithospheric plumbing system that conducts magma to shallow levels. Finally, the resulting shallow-level magma distribution determines which parts of a spreading segment will be subjected to greater or lesser tectonic extension.

Any of these controls may have greater or lesser importance at a given MOR. In the slow-spreading crust of our study area the magma supply from the asthenosphere appears to be highly 3D in location and thus may determine primary segmentation, but it appears not to vary significantly in volume so the shallower, lithospheric effects assume greater importance in controlling NTD evolution. In contrast, as noted earlier, the much greater magma supply in the TAMMAR segment (Dannowski et al., 2011) may overwhelm shallow lithospheric effects.

The schematic model in Figure 14 summarizes, for segments A, E, and G and the two intervening NTDs, the possible effects of the three factors noted above. For simplicity, the model assumes that magma production is controlled by compositional heterogeneity of the mantle, but dynamic upwelling, whether or not enhanced by buoyancy that results from melting in zones of fertile mantle, would produce similar effects. The model depicts only the gross long-term trends over the past ~25 Myr. It assumes a heterogeneous mantle in which parcels of enriched mantle rise beneath the ridge axis, melt at shallow levels, and produce magma to form new oceanic crust. The model is both a hindcast (horizontal surface) and forecast (vertical front surface) of NTD propagation in response to gross volume and distribution of magma; the forecast is based on interpreted trends of NTD and segment evolution up to the present.

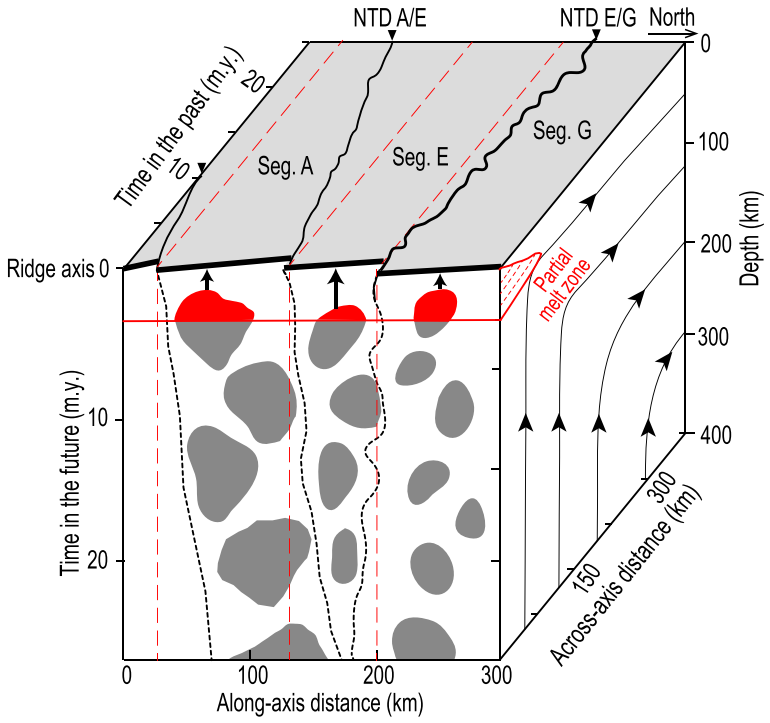

Figure 14. Schematic 3-D model of melt supply among segments A, E, and G during seafloor spreading, with corresponding nontransform discontinuity (NTD) evolution. Right panel: Mantle flowlines are shown as black lines, and the partial melt zone is in red (based on the model of Behn & Grove, 2015). Top panel: Propagation of segments A, E, and G and intervening NTDs (black lines) is shown for the past ~25 Myr; red dashed lines are flowlines of relative plate motion. Front panel: Regions of fertile mantle (gray) are shown with respect to future plate flowlines (red dashes); although depicted as fertile mantle, these regions could also be considered as future zones of dynamic upwelling. The black dashed lines are future NTD boundaries. The assumed average half spreading rate is 15 mm/year. The locations, volumes, and distributions of future sources of magma within each segment represent continuations of the pattern of magma sources that we infer have controlled the evolution of segments and intervening NTDs over the past ~25 Myr. We infer that NTD A/E has propagated northward due to a combination of three factors: (1) northward displacement of fertile source mantle with depth in segment A, (2) slightly greater volume of fertile mantle in segment A compared to segment E, and (3) low magma supply (and thus enhanced extension) in the northern part of segment A compared to segment E. NTD E/G has propagated southward because the southern part of segment G has lower magma supply (thus enhanced extension) compared to adjacent segment E. If these patterns continue, segment E will disappear in the future.

Persistent northward propagation of NTD A/E in Figure 14 is attributed to a combination of all three factors, each of which may have been more or less important than the other two through time. Average magma volume in segment A is slightly greater than in segment E, its enriched-source mantle is progressively farther north with depth, and magma deposition is shifted toward the south within the segment, leaving the northern part magma-deficient and thus subject to increased extension compared to the adjacent southern part of segment E.

Southward propagation of NTD E/G is attributed to lower magma supply in segment G than in segment E. The resulting increased tectonic extension in the southern part of segment G compared to segment E drives the propagation. Continuation of the trends in NTD propagation would eventually lead to the demise of segment E. The evolution of NTD G/H at the northern margin of segment G is ignored in this schematic model.

The schematic model does not depict rapid propagation of NTDs that have small ridge-axis offsets comparable to the width of the central rift. Such propagation is attributed primarily to reduced magma supply and enhanced tectonic extension within the shallow lithosphere of an entire segment; this drives propagation into an adjacent, somewhat more magmatic segment.

5.4. Long-Term RMBA Asymmetry

RMBA gravity varies at both short periods (3–4 Myr) and long periods (>5–10 Myr) in our study area (Figures 1b and 11), and we ascribe these changes to time-dependent variations in magma supply beneath

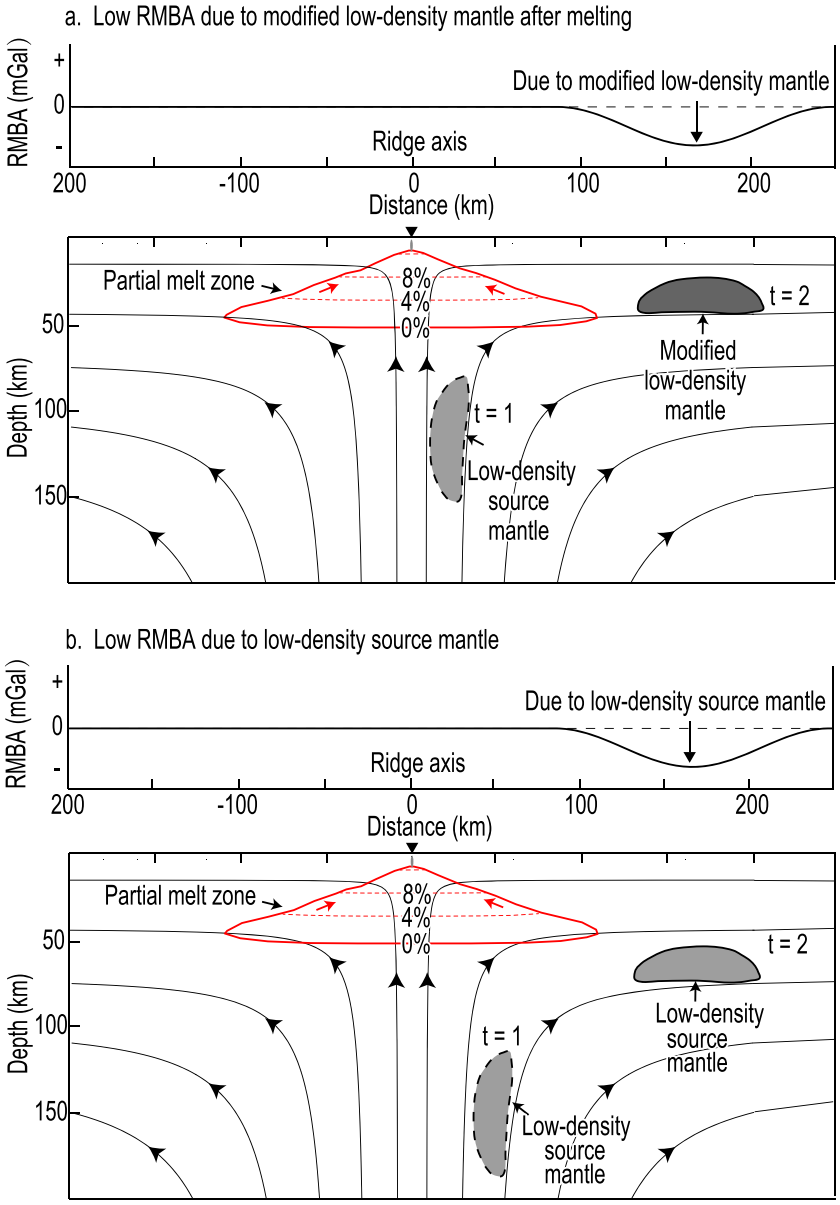

Figure 15. Two possible cross-ridge models that could explain observed long-period residual mantle Bouguer anomaly (RMBA) asymmetry on the flanks of the Mid-Atlantic Ridge (MAR). (a) A region of low-density source mantle (gray) rises near, but to the side of the ridge axis (time t1) and passes through the melt zone (red contours with melt percentage indicated). At time t2 the region has passed through the melt zone and its density is modified depending on the degree of melting (dark gray); RMBA shows the effect of this modified low-density source as a broad gravity low. (b) A region of low-density mantle (gray) rises off-axis (time t1) and does not pass through the melt zone (time t2). The low density is recorded by reduced RMBA. In both cases, observed reduction of RMBA depends on the size, shape, and depth of the anomalous region at t2, as well as its density compared to the surrounding mantle. Flowlines (black lines with arrows) and melt zone (red, with melting percentage) are based on the model of Behn and Grove (2015).

the ridge axis (Figure 14). An unusual feature of the longer-wavelength RMBA in several locations is that it is not symmetrical across the ridge axis (Figure 11). RMBA on the east flank of segment I has been up to 20 mGal more positive than that on the west flank over the past 8–10 Myr, and significant asymmetries are present over somewhat shorter time scales in 2- to 8-Ma crust of the other segments. Large asymmetries are also present farther off-axis in crust older than about 13 Ma in segment G and older than 18 Ma in segment H2. These asymmetries have previously been interpreted to be the result of changing magma input at the ridge axis interacting with asymmetric normal faulting (Wang et al., 2015). This may explain

long-wavelength differences in RMBA between the conjugate ridge flanks over the past ~8 Myr and may also explain the asymmetrically elevated RMBA at ~19–17 Ma on the west flank of segment G where core complexes were exhumed by detachment faulting. However, it seems unlikely that they explain the long-wavelength RMBA difference between conjugate ridge flanks at ~17 to ~13 Ma in segment G and older than 18 Ma in segment H2 (Figures 1b and 11) because there are no significant differences in fault patterns on the two flanks. Here we suggest an alternate, deeper mantle explanation for the RMBA difference in the older lithosphere of segments G and H2; it may also explain, or contribute to, the difference in younger, <8-Ma lithosphere.

In Figure 15 we show how large-scale density anomalies in the deep mantle could create long-wavelength differences in RMBA on the two ridge flanks. The key feature is that these density anomalies are not centered beneath the ridge axis. In the first model (Figure 15a), an off-axis region of low-density source mantle is rising and will pass through the melting zone beneath the ridge axis (time $t = 1$). Based on Behn and Grove (2015), the melting zone is expected to extend to ~100 km from the axis along the spreading direction and to reach ~50-km depth at a 30 mm/year full spreading rate, comparable to the rate of 26–32 mm/year within our study area. After it has passed through the melting zone (time $t = 2$), the low-density mantle source region will be further depleted but will maintain its lower density relative to the surrounding, partially melted normal mantle, thus producing a long-wavelength negative RMBA.

In the second model (Figure 15b), a region of lower-density mantle material is located farther off-axis (time $t = 1$). With time, it reaches the upper mantle, following mantle flowlines, but it does not pass through the melting zone (time $t = 2$). The region remains entirely beneath the east ridge flank and somewhat deeper in the mantle, and it produces a long-wavelength negative gravity anomaly. In both cases, the observed negative gravity anomaly depends on the shape, size, depth, and density contrast of the lower-density mantle region.

Because the MAR plate boundary is migrating westward in the hotspot reference frame (Gripp & Gordon, 2002), another possibility is that low-density mantle anomalies that are either inherent in the mantle or that develop from deep melting become asymmetrically distributed to beneath the eastern ridge flank. If this were the case, we would expect systematically lower RMBA values all along the African plate east of the MAR. As shown by Wang et al. (2011), however, low RMBA values are randomly distributed over large areas on both sides of the ridge. Thus, we suggest that just as potentially magma-producing mantle regions can be randomly distributed along-axis (Figure 14), they can also be asymmetrically distributed across the ridge axis, leading to significant asymmetry in RMBA on conjugate ridge flanks. This phenomenon may be more common than has previously been recognized.

6. Conclusions

We analyzed the structure and long-term evolution of non-NTDs on the slow-spreading MAR using plate reconstructions of non-isostatic topography, RMBA, long-range sidescan sonar, and gravity-derived crustal thickness. The analyses yield the following conclusions:

1. NTDs generally are bounded by well developed IC/OC structure, that is, elevated and often irregularly faulted IC crust with high RMBA, and deeper OC crust with lineated abyssal hills and low RMBA. The NTDs have propagated both north and south along the ridge axis over the past ~24 Myr, they have merged and reappeared, they have changed offset, and they have persisted even when the sense of offset reversed.
2. Small-scale (<10–15 km), short-term (<1 Myr) propagation to the north or south occurs frequently within the typical width (<25 km) of an NTD, capturing edifices or septa that develop between offset ridge tips and transferring them intermittently to one ridge flank or the other. This process creates the typical, irregular off-axis traces of the axes of maximum depth of NTDs.
3. Larger-scale and/or longer-term propagation of NTDs occurs at rates ranging from ~2.4 to 66.3 km/Myr (i.e., 17–265% of the half spreading rate). The fastest propagators move at rates greater than the half spreading rate and have ridge-axis offsets less than ~5 km, comparable to the width of the central rift between the first major bounding faults at the sides of the rift axis. They are characterized by elevated RMBA in the propagating rift compared to the doomed rift. We interpret the elevated RMBA to mean that the crust is thinner, and thus, extension is greater in the propagating rift, which drives the propagating rift tip into the doomed rift. These fast propagators do not show obvious morphological features that indicate transfer of crust from one ridge flank to the other.

4. NTDs propagating at rates slower than the half spreading rate usually, but not always, have offsets larger than the width of the central rift (~5–10 km), indicating that the thermal barrier of larger offsets can be effective in hindering propagation. Three of the slower propagators exhibit classic propagating rift features, that is, inner and outer pseudofaults, failed rift, and transferred crustal blocks. Crustal transfer from one ridge flank to the other is limited to within the confines of the NTD valley. Propagation appears to be largely discontinuous, occurring every 1–4 Myr during intervals of reduced magmatism that follow intermittent construction of volcanic edifices within the NTD. The propagating rift tip consistently has higher RMBA than the doomed rift, irrespective of gross magma supply within the propagating segment, indicating that the increased extension at the ridge tip drives propagation. Thus, the distribution of magma within a ridge segment, controlled by the lithospheric, intrasegment magma plumbing system, is important in determining whether the bounding NTD will propagate.
5. For the conditions in our study area, the difference in average crustal thickness ($\lesssim$900 m) and thus gross magma supply between adjacent ridge segments is too small to affect NTD propagation significantly. However, very large crustal-thickness differences are known to drive propagation in other areas, even in the presence of a large offset (e.g., the TAMMAR segment south of Kane Fracture Zone, Dannowski et al., 2011). Thus, we infer that differential magma supply between segments can drive propagation, but only if the magnitude of the differential is great enough to overcome the thermal-barrier effect of the NTD offset.
6. An important factor that may influence NTD propagation is the shifting locations of zones of fertile mantle, dynamic upwelling, or a combination of both beneath the ridge axis. As these zones rise, melt, and supply magma to the crust, their positions can cause spreading segments to migrate, thus driving propagation at the bounding NTDs.
7. We conclude that NTD propagation in slow-spreading crust results from a complex, variable, and tiered interplay between several factors, extending from the asthenosphere to the crust: (1) The volume, location, and time-dependent shifts of magma supplied from the asthenosphere by melting of zones of fertile mantle and/or dynamic upwelling; this controls the gross segmentation of the MAR. Very large differences in magma supply between adjacent spreading segments can drive propagation. (2) The intrasegment distribution of magma along the ridge axis as controlled by the lithospheric plumbing system. (3) The resulting distribution of magmatic vs. tectonic extension within a spreading segment; enhanced extension within or at the end of a segment can drive propagation into an adjacent segment. In addition, increase of ridge-axis offset lengths in NTDs beyond the width of the central rift tends to inhibit ridge-tip propagation. All of these factors, to a greater or lesser extent, ultimately are controlled by the distribution of melting potential of the mantle beneath the ridge axis at the subsegment to segment scale.
8. In addition to short-wavelength variations in RMBA associated with spreading segments and NTDs, we observe long-wavelength (~5–10 Myr) asymmetry in RMBA on conjugate flanks of the MAR. We propose that these differences reflect asymmetric distribution of density differences in the underlying mantle. Just as zones of fertile or depleted mantle can be distributed "randomly" along the ridge axis, zones of density anomalies in the mantle can also be distributed asymmetrically across the ridge axis.

Acknowledgments
We thank Tingting Wang for providing plate-reconstruction codes, Ross Parnell-Turner for technical support, and Anouk Beniest and an anonymous reviewer for comments that helped to improve the manuscript. We benefited greatly from discussion with the Deep Sea Geodynamics Group of the South China Sea Institute of Oceanology. Figures were drawn using the GMT software of Wessel and Smith (1998). This study was supported by National Natural Science Foundation of China (91628301, 41890813, and U1606401), Chinese Academy of Sciences (Y4SL021001, QYZDY-SSW-DQC005, and 133244KYSB20180029), Chinese National 985 Project (1350141509), International Exchange Program for Graduate Students of Tongji University (2016020006), China Scholarship Council (201706260034), and Woods Hole Oceanographic Institution. We thank the crews and science parties of the ARSRP, MAREAST, MODE94, and MODE98 expeditions for their contributions to data acquisition. ARSRP and MAREAST data acquisition was funded by Office of Naval Research grant N00014-90-J-6121 and by U.S. National Science Foundation grant OCE-9503561, respectively. Access to the original data used in this study is available at https://doi.org/10.26025/z2z7-kd89.

References

Behn, M. D., & Grove, T. L. (2015). Melting systematics in mid-ocean ridge basalts: Application of a plagioclase-spinel melting model to global variations in major element chemistry and crustal thickness. *Journal of Geophysical Research: Solid Earth*, *120*, 4863–4886. https://doi.org/10.1002/2015JB011885

Briais, A., Aslanian, D., Géli, L., & Ondréas, H. (2002). Analysis of propagators along the Pacific–Antarctic Ridge: Evidence for triggering by kinematic changes. *Earth and Planetary Science Letters*, *199*(3-4), 415–428. https://doi.org/10.1016/S0012-821X(02)00567-8

Brozena, J. M., & White, R. S. (1990). Ridge jumps and propagations in the South Atlantic Ocean. *Nature*, *348*(6297), 149–152. https://doi.org/10.1038/348149a0

Cannat, M., Mevel, C., Maia, M., Deplus, C., Durand, C., Gente, P., et al. (1995). Thin crust, ultramafic exposures, and rugged faulting patterns at the Mid-Atlantic Ridge (22°–24°N). *Geology*, *23*(1), 49–52. https://doi.org/10.1130/0091-7613(1995)023<0049:TCUEAR>2.3.CO;2

Dannowski, A., Grevemeyer, I., Phipps Morgan, J., Ranero, C. R., Maia, M., & Klein, G. (2011). Crustal structure of the propagating TAMMAR ridge segment on the Mid-Atlantic Ridge, 21.5°N. *Geochemistry, Geophysics, Geosystems*, *12*, Q07012. https://doi.org/10.1029/2011GC003534

Dannowski, A., Morgan, J. P., Grevemeyer, I., & Ranero, C. R. (2018). Enhanced mantle upwelling/melting caused segment propagation, oceanic core complex die off, and the death of a transform fault: The Mid-Atlantic Ridge at 21.5°N. *Journal of Geophysical Research: Solid Earth*, *123*, 941–956. https://doi.org/10.1002/2017JB014273

Escartín, J., & Lin, J. (1995). Ridge offsets, normal faulting, and gravity anomalies of slow spreading ridges. *Journal of Geophysical Research*, *100*(B4), 6163–6177. https://doi.org/10.1029/94JB03267

Fujimoto, H., Seama, N., Lin, J., Matsumoto, T., Tanaka, T., & Fujioka, K. (1996). Gravity anomalies of the Mid-Atlantic Ridge north of the Kane Fracture Zone. *Geophysical Research Letters*, *23*(23), 3431–3434. https://doi.org/10.1029/96GL02080

Fujioka, K., Chiba, H., Naganuma, T., Masuda, H., Oomori, T., Rona, P. A., et al. (1999). Hydrothermal activity and architecture of slow-spreading ridge at TAG and Rainbow hydrothermal fields and Dante's Domes megamullion in the Mid-Atlantic Ridge – MODE'98 Leg 2 MEGATRAIN cruise results summary. *JAMSTEC Journal of Deep Sea Research*, *15*, 39–49.

Gente, P., Pockalny, R. A., Durand, C., Deplus, C., Maia, M., Ceuleneer, G., et al. (1995). Characteristics and evolution of the segmentation of the Mid-Atlantic Ridge between 20°N and 24°N during the last 10 million years. *Earth and Planetary Science Letters*, *129*(1-4), 55–71. https://doi.org/10.1016/0012-821X(94)00233-O

Gràcia, E., Bideau, D., Hekinian, R., Lagabrielle, Y., & Parson, L. M. (1997). Along-axis magmatic oscillations and exposure of ultramafic rocks in a second-order segment of the Mid-Atlantic Ridge (33°43′N to 34°07′N). *Geology*, *25*(12), 1059–1062. https://doi.org/10.1130/0091-7613(1997)025<1059:AAMOAE>2.3.CO;2

Gràcia, E., Charlou, J. L., Radford-Knoery, J., & Parson, L. M. (2000). Non-transform offsets along the Mid-Atlantic Ridge south of the Azores (38°N–34°N): ultramafic exposures and hosting of hydrothermal vents. *Earth and Planetary Science Letters*, *177*(1-2), 89–103. https://doi.org/10.1016/S0012-821X(00)00034-0

Gripp, A. E., & Gordon, R. G. (2002). Young tracks of hotspots and current plate velocities. *Geophysical Journal International*, *150*(2), 321–361. https://doi.org/10.1046/j.1365-246X.2002.01627.x

Hey, R. (1977). A new class of "pseudofaults" and their bearing on plate tectonics: A propagating rift model. *Earth and Planetary Science Letters*, *37*(2), 321–325. https://doi.org/10.1016/0012-821X(77)90177-7

Hey, R., Duennebier, F. K., & Morgan, W. J. (1980). Propagating rifts on mid-ocean ridges. *Journal of Geophysical Research*, *85*(B7), 3647–3658. https://doi.org/10.1029/JB085iB07p03647

Hey, R., Kleinrock, M., Miller, S., Atwater, T., & Searle, R. (1986). Sea Beam/Deep-Tow investigation of an active oceanic propagating rift system, Galapagos 95.5°W. *Journal of Geophysical Research*, *91*(B3), 3369–3393. https://doi.org/10.1029/JB091iB03p03369

Hey, R., Martinez, F., Höskuldsson, Á., & Benediktsdóttir, Á. (2010). Propagating rift model for the V-shaped ridges south of Iceland. *Geochemistry, Geophysics, Geosystems*, *11*, Q03011. https://doi.org/10.1029/2009GC002865

Kleinrock, M. C., & Hey, R. (1989). Detailed tectonics near the tip of the Galapagos 95.5°W propagator: How the lithosphere tears and a spreading axis develops. *Journal of Geophysical Research*, *94*(B10), 13,801–13,838. https://doi.org/10.1029/JB094iB10p13801

Kleinrock, M. C., Tucholke, B. E., Lin, J., & Tivey, M. A. (1997). Fast rift propagation at a slow-spreading ridge. *Geology*, *25*(7), 639–642. https://doi.org/10.1130/0091-7613(1997)025<0639:FRPAAS>2.3.CO;2

Klitgord, K., & Schouten, H. (1986). Plate kinematics of the central Atlantic. In P. R. Vogt, & B. E. Tucholke (Eds.), *The Geology of North America, The Western North Atlantic Region*, (Vol. M, pp. 351–378). Boulder, Colorado: Geological Society of America.

Lin, J., & Phipps Morgan, J. (1992). The spreading rate dependence of three-dimensional mid-ocean ridge gravity structure. *Geophysical Research Letters*, *19*(1), 13–16. https://doi.org/10.1029/91GL03041

Lin, J., Purdy, G. M., Schouten, H., Sempere, J. C., & Zervas, C. (1990). Evidence from gravity data for focused magmatic accretion along the Mid-Atlantic Ridge. *Nature*, *344*(6267), 627–632. https://doi.org/10.1038/344627a0

Lin, J. & Zhu, J. (2015). Global variations in gravity-derived oceanic crustal thickness and implications on oceanic crustal accretion processes (V14A-07). Paper presented at AGU Fall Meeting, San Francisco, CA.

Macdonald, K., Scheirer, D., & Carbotte, S. (1991). Mid-ocean ridges: Discontinuities, segments and giant cracks. *Science*, *253*(5023), 986–994. https://doi.org/10.1126/science.253.5023.986

Macdonald, K. C., Fox, P., Perram, L., Eisen, M., Haymon, R., Miller, S., et al. (1988). A new view of the mid-ocean ridge from the behaviour of ridge-axis discontinuities. *Nature*, *335*(6187), 217–225. https://doi.org/10.1038/335217a0

Magde, L. S., Barclay, A. H., Toomey, D. R., Detrick, R. S., & Collins, J. A. (2000). Crustal magma plumbing within a segment of the Mid-Atlantic Ridge, 35°N. *Earth and Planetary Science Letters*, *175*(1), 55–l67. https://doi.org/10.1016/S0012-821X(99)00281-2

Ogg, J. G. (2012). Geomagnetic polarity time scale. In F. M. Gradstein, et al. (Eds.), *The Geologic Time Scale 2012*, (pp. 85–113). Amsterdam, Netherlands: Elsevier B. V. https://doi.org/10.1016/B978-0-444-59425-9.00005-6

Parson, L., Gràcia, E., Coller, D., German, C., & Needham, D. (2000). Second-order segmentation; the relationship between volcanism and tectonism at the MAR, 38°N–35°40′N. *Earth and Planetary Science Letters*, *178*(3-4), 231–251. https://doi.org/10.1016/S0012-821X(00)00090-X

Parson, L., & Hawkins, J. (1994). Two-stage ridge propagation and the geological history of the Lau Backarc Basin. In *Proceedings of the Ocean Drilling Program, Scientific Results*, (Vol. 135, pp. 819–828). College Station, TX: Ocean Drilling Program.

Paulatto, M., Canales, J. P., Dunn, R. A., & Sohn, R. A. (2015). Heterogeneous and asymmetric crustal accretion: New constraints from multibeam bathymetry and potential field data from the Rainbow area of the Mid-Atlantic Ridge (36°15'N). *Geochemistry, Geophysics, Geosystems*, *16*, 2994–3014. https://doi.org/10.1002/2015GC005743

Pollard, D. D., & Aydin, A. (1984). Propagation and linkage of oceanic ridge segments. *Journal of Geophysical Research*, *89*(B12), 10,017–10,028. https://doi.org/10.1029/JB089iB12p10017

Purdy, G., Sempere, J.-C., Schouten, H., Dubois, D., & Goldsmith, R. (1990). Bathymetry of the Mid-Atlantic Ridge, 24°– 31°N: A map series. *Marine Geophysical Researches*, *12*(4), 247–252. https://doi.org/10.1007/BF02428196

Rognstad, M. (1992), Hawaii MR1: A new underwater mapping tool. Paper presented at International Conference on Signal Processing and Technology (pp. 900-905), San Francisco, CA.

Rona, P. A., & Gray, D. F. (1980). Structural behavior of fracture zones symmetric and asymmetric about a spreading axis: Mid-Atlantic Ridge (latitude 23°N to 27°N). *Geological Society of America Bulletin*, *91*(8), 485–494. https://doi.org/10.1130/0016-7606(1980)91<485:SBOFZS>2.0.CO;2

Sandwell, D. T., Müller, R. D., Smith, W. H., Garcia, E., & Francis, R. (2014). New global marine gravity model from CryoSat-2 and Jason-1 reveals buried tectonic structure. *Science*, *346*(6205), 65–67. https://doi.org/10.1126/science.1258213

Schouten, H., Klitgord, K. D., & Whitehead, J. A. (1985). Segmentation of mid-ocean ridges. *Nature*, *317*(6034), 225–229. https://doi.org/10.1038/317225a0

Sempéré, J. C., Lin, J., Brown, H. S., Schouten, H., & Purdy, G. M. (1993). Segmentation and morphotectonic variations along a slow-spreading center: The Mid-Atlantic Ridge (24°00′N–30°40′N). *Marine Geophysical Researches*, *15*(3), 153–200. https://doi.org/10.1007/BF01204232

Sempéré, J. C., Purdy, G. M., & Schouten, H. (1990). Segmentation of the Mid-Atlantic Ridge between 24°N and 30°40'N. *Nature*, *344*(6265), 427–431. https://doi.org/10.1038/344427a0

Shaw, W. J., & Lin, J. (1996). Models of ocean ridge lithospheric deformation: Dependence on crustal thickness, spreading rate, and segmentation. *Journal of Geophysical Research*, *101*(B8), 17,977–17,994. https://doi.org/10.1029/96JB00949

Smith, D. K., & Cann, J. R. (1993). Building the crust at the Mid-Atlantic Ridge. *Nature*, *365*, 707–715.
Spencer, S., Smith, D. K., Cann, J. R., Lin, J., & Mcallister, E. (1997). Structure and stability of non-transform discontinuities on the Mid-Atlantic Ridge between 24°N and 30°N. *Marine Geophysical Researches*, *19*(4), 339–362. https://doi.org/10.1023/A:1004200411959
Tivey, M., Takeuchi, A., & Party, W. S. (1998). A submersible study of the western intersection of the Mid-Atlantic ridge and Kane fracture zone (WMARK). *Marine Geophysical Researches*, *20*(3), 195–218. https://doi.org/10.1023/A:1004630501837
Tivey, M. A., & Tucholke, B. E. (1998). Magnetization of 0–29 Ma ocean crust on the Mid-Atlantic Ridge, 25°30′ to 27°10′N. *Journal of Geophysical Research*, *103*(B8), 17,807–17,826. https://doi.org/10.1029/98JB01394
Tucholke, B. E., Fujioka, K., Ishihara, T., Hirth, G., & Kinoshita, M. (2001). Submersible study of an oceanic megamullion in the central North Atlantic. *Journal of Geophysical Research*, *106*(B8), 16,145–16,161. https://doi.org/10.1029/2001JB000373
Tucholke, B. E., Kleinrock, M. C., & Lin, J. (1996). *Ewing Cruise 9606 Mid-Atlantic Ridge East Flank (MAREAST Survey) (Cruise Report, 71 pp.)*. Woods Hole, MA: Woods Hole Oceanographic Institution.
Tucholke, B. E., & Lin, J. (1994). A geological model for the structure of ridge segments in slow spreading ocean crust. *Journal of Geophysical Research*, *99*(B6), 11,937–11,958. https://doi.org/10.1029/94JB00338
Tucholke, B. E., Lin, J., Kleinrock, M. C., Tivey, M. A., Reed, T. B., Goff, J., & Jaroslow, G. E. (1997). Segmentation and crustal structure of the western Mid-Atlantic Ridge flank, 25°25′-27°10′N and 0-29 m.y. *Journal of Geophysical Research*, *102*(B5), 10,203–10,223. https://doi.org/10.1029/96JB03896
Tucholke, B. E., & Schouten, H. (1988). Kane Fracture Zone. *Marine Geophysical Researches*, *10*(1), 1–39. https://doi.org/10.1007/BF02424659
Vogt, P. R. (1986). Magnetic anomalies and crustal magnetization. In P. R. Vogt, & B. E. Tucholke (Eds.), *The Geology of North America, The Western North Atlantic Region* (Vol. M, pp. 229–256). Boulder, Colorado: Geological Society of America.
Wang, T., Lin, J., Tucholke, B., & Chen, Y. J. (2011). Crustal thickness anomalies in the North AtlanticOcean basin from gravity analysis. *Geochemistry, Geophysics, Geosystems*, *12*, Q0AE02. https://doi.org/10.1029/2010GC003402
Wang, T., Tucholke, B. E., & Lin, J. (2015). Spatial and temporal variations in crustal production at the Mid-Atlantic Ridge, 25°N-27°30′N and 0-27 Ma. *Journal of Geophysical Research: Solid Earth*, *120*, 2119–2142. https://doi.org/10.1002/2014JB011501
Wessel, P., & Smith, W. H. (1998). New, improved version of Generic Mapping Tools released. *Eos, Transactions American Geophysical Union*, *79*(47), 579–579. https://doi.org/10.1029/98EO00426
Wetzel, L. R., Wiens, D. A., & Kleinrock, M. C. (1993). Evidence from earthquake for bookshelf faulting at large non-transform ridge offsets. *Nature*, *362*(6417), 235–237. https://doi.org/10.1038/362235a0
Wilson, D. S., Hey, R. N., & Nishimura, C. (1984). Propagation as a mechanism of reorientation of the Juan de Fuca Ridge. *Journal of Geophysical Research*, *89*(B11), 9215–9225. https://doi.org/10.1029/JB089iB11p09215
Zonenshain, L., Kuzmin, M., Lisitsin, A., Bogdanov, Y. A., & Baranov, B. (1989). Tectonics of the Mid-Atlantic rift valley between the TAG and MARK areas (26–24 N): Evidence for vertical tectonism. *Tectonophysics*, *159*(1-2), 1–23. https://doi.org/10.1016/0040-1951(89)90167-4